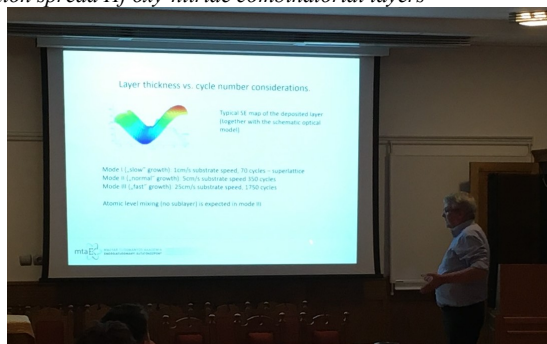# Symposium on Materials Science
Mátraháza, Hungary, September 23-25, 2020
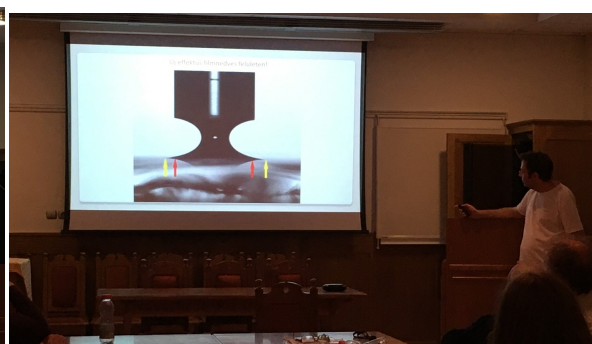### Organizing and Programme Committee:
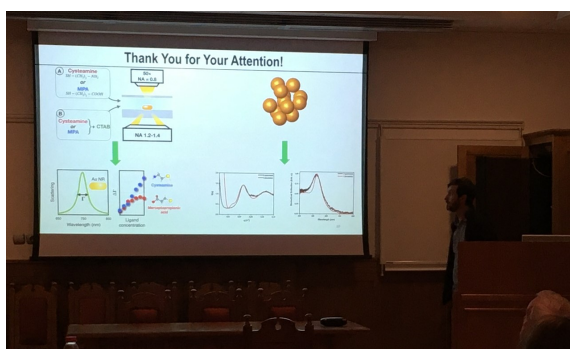### Miklós Fried (ed.), Ákos Nemcsics, Attila Bonyár, Péter Petrik, András Deák
EK MFA, ÓE KVK, BME
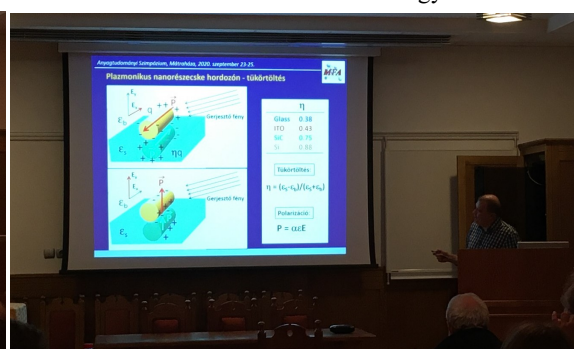
Lecturers: Zoltán Lábadi
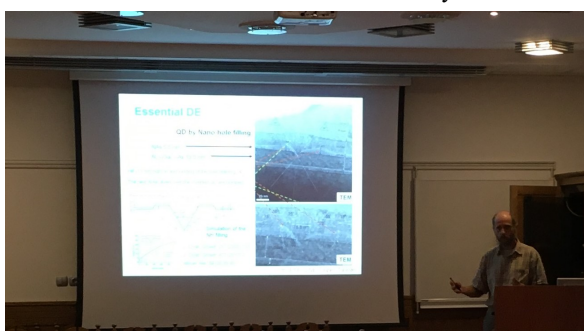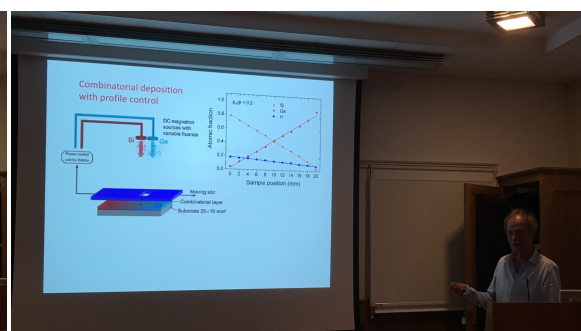

Norbert Nagy

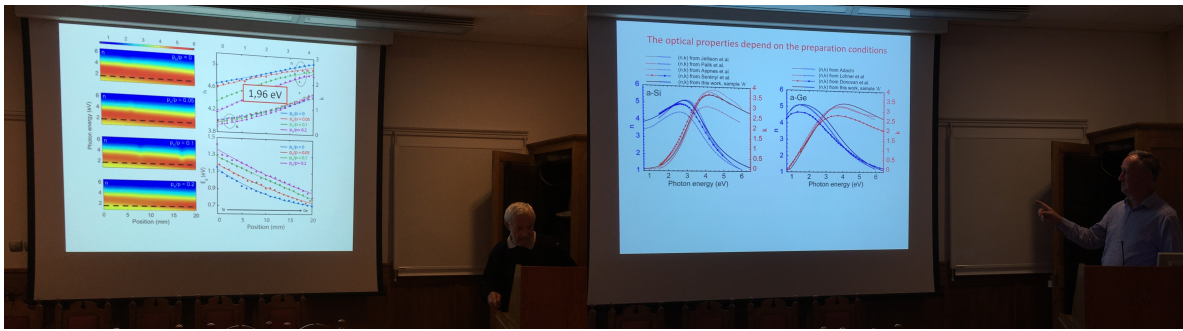Lecturers: Dániel Péter Szekrényes

Zsolt Zolnai

Lecturers: Ákos Nemcsics

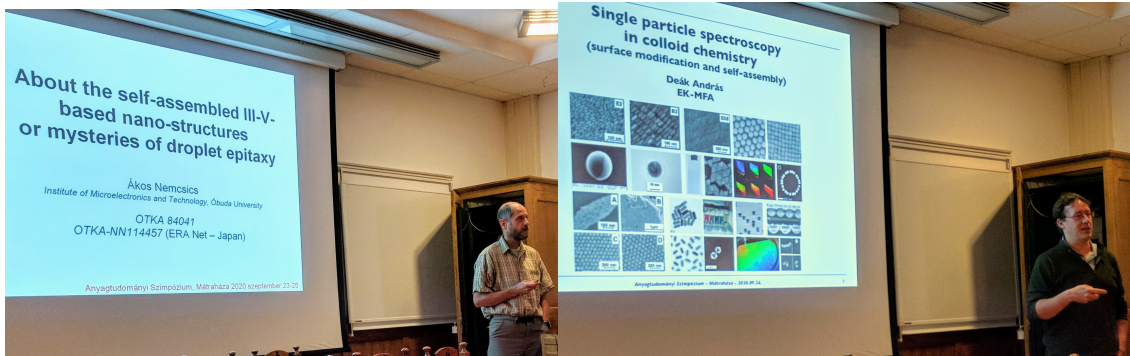György Sáfrán

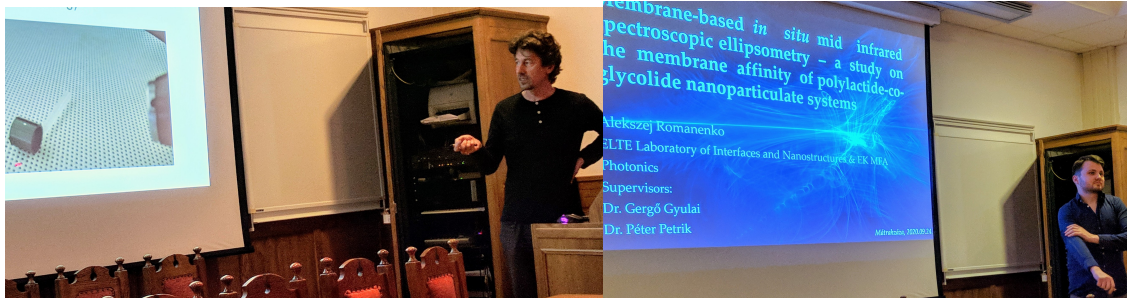Lecturers: Miklós Serényi   Miklós Fried

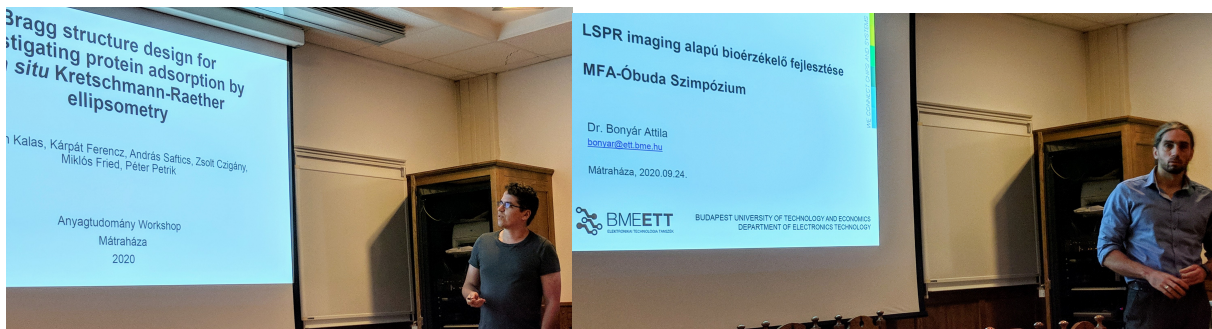Lecturers: Ákos Nemcsics   András Deák

Lecturers: Péter Petrik   Alekszej Romanenko

Lecturers: Benjamin Kalas   Attila Bonyár

Combinatorial Investigation of WO₃-MoO₃ Mixed Layers by Spectroscopic Ellipsometry to assess Effective Medium Approximation

M. Fried[a,b], R. Bogar[a], Z. Lábadi[b], Z. E. Horvath[b], Z. Zolnai[b],

a Institute of Microelectronics and Technology, Óbuda University, Tavaszmezo u. 17, H-1084 Budapest, Hungary

b Institute of Technical Physics and Materials Science, Centre for Energy Research, Hungarian Academy of Sciences, P.O. Box 49, H-1525 Budapest, Hungary

Keywords: thim films, combinatorial preparation, spectroscopic ellipsometry

Currently, the protection against heat waves through the glass windows, the electrochromic film as a smart window [1] is the most useful tool to reduce heat in buildings. This type of glass consists of a layer of electrochromic film bounded by metal oxide layers. It controls the transmitted amount of light by supplying electric charge to the film system. There are many types of such as TiO_2, CrO, Nb_2O_5, SnO_2, NiO, IrO_2 [2], WO_3, and MoO_3 [3, 4]. Researchers have different methods of deposition as sputtering [5], atmospheric pressure chemical vapor deposition (APCVD) [6], dipping [7], sol-gel method [1, 4], and sintering [8]. This later paper investigated mixed materials but only limited number of compositions: $(MoO_3)_x$ - $(WO_3)_{1-x}$ for x=0, 0.2, 0.4, 0.6, 0.8.

During the present work we used reactive (in $Ar-O_2$ plasma) magnetron sputtering to create all combinations of WO₃-MoO₃ mixed layers along a line/band. Using combinatorial approach, we have all the compositions after one sputtering process in the same sputtering chamber. Our further aim is to investigate the goodness of WO₃-MoO₃ mixed layers as electrochromic materials for „smart" windows (transparency ratio, switching speed, coloration efficiency).

Layer depositions were performed in a reactive ($Ar + O_2$) gas mixture in high vacuum ($\sim 2 \times 10^{-6}$ mbar base and $\sim 10^{-3}$ mbar process pressure). 30 sccm/sec Ar and 30 sccm/sec O_2 volumetric flow rate was applied in the magnetron sputtering chamber. The substrates were 30 cm * 30 cm soda lime glasses. First, a W-mirror (W sputtered only in Ar-plasma) was prepared to avoid the back-reflection of the measuring light-beam during the Spectroscopic Ellipsometry (SE) measurements. The plasma powers of the two targets were chosen in the 0.75-1.5 kW range independently. We used 1, 5 or 25 cm/sec walking speed (back and forth) which was the speed of the 30x30 cm glass sample between the end positions (the edges of the targets).

The sputtering targets were placed in two arrangements as it can be seen in Fig. 1. In the first arrangement, the two targets were placed at 35 cm, in the second arrangement they were placed at 70 cm distance from each other. According to the measurements, in the first arrangement the two „material streams" overlapped around the center position, while in the second arrangement the two „material streams" were separated.
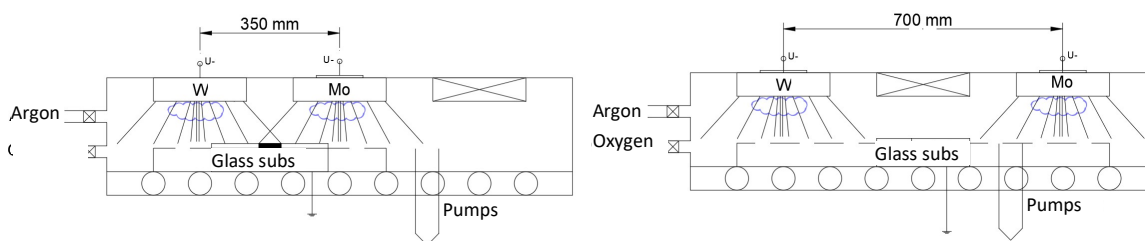
Fig 1 Two arrangements of the targets: a) the two targets in closer position (35 cm from each other) b) the two targets in distant position (70 cm from each other).

We used a Woollam M2000 SE device [9] to map the thickness and the composition change. We used CompleteEASE program (from Woolam Co., https://www.jawoollam.com/ellipsometry-software/completeease) to evaluate the mapping measurements using the built-in optical models and oscillator functions: Tauc-Lorentz (T-L) oscillators or Effective Medium Approximation. Note, that the maps from the M2000 measurements are compiled from four 15*15 cm parts. Our M2000 device can measure only one 15*15 cm part at once. The mapping measurements were performed with mm-sized beam-spot on a 15x15 grid with one spectra-pair per cm!

After sputtering, we investigated and mapped the samples by Spectroscopic Ellipsometry (SE) which is a relatively quick, cheap and a contactless method. We used different (oscillator- and Effective Medium Approximation, EMA-based) optical models to obtain the thickness and composition map of the sample layer. We checked the SE results using Rutherford Backscattering Spectrometry. In a set of experiments, we changed the position of the sputtering targets, the speed and cycle number of the substrate motion. Our aim was to compare the "goodness" of the different optical models depending upon the sample preparation conditions.

We used Si-probes which were placed at the centre line (6x5 cm long) of some samples for Rutherford Backscattering Spectrometry (RBS, see Fig. 4) and X-ray Diffractometry (XRD) measurements.

We used the Tauc-Lorentz oscillator model (Fig. 2) which is built-in (CompleteEASE program) and can be used as pre-determined component in the Bruggeman's Effective Medium Approximation (EMA or B-EMA [12]). In the EMA calculation, the mixed-layer is considered as being a physical combination of two distinct phases formed by WO_3 and MoO_3 with an appropriate volume fraction. The constituents are considered equivalent – neither of the components is considered as a host material. In this case, it holds that

$$0 = \sum_i^N f_i \frac{\varepsilon_i - \varepsilon}{\varepsilon_i + 2\varepsilon}$$

where ε is the effective complex dielectric function of the composite layer; f_i and ε_i denote volume fraction and the complex dielectric function of the ith component. In the case of two components, (WO_3 and MoO_3) the formula is a complex quadratic equation where ε (the effective dielectric function) is the unknown and we can choose easily between the two solutions. (The wrong one is physically meaningless.)
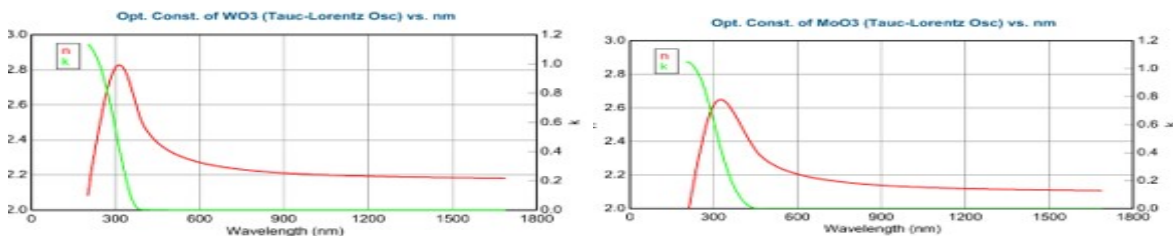
Fig. 2 Determined complex refractive indices using the Tauc-Lorentz oscillator model for pure WO₃ (left) and MoO₃ (right)

The Tauc-Lorentz (T-L) oscillator model is a combination of the Tauc and Lorentz models [11] T-L model contains 4 parameters: the transition Amplitude, the Broadening coefficient of the Lorentz oscillator, the peak position for the Lorentz oscillator, and the Bandgap Energy (Eg), which is taken to be the photon energy where $\varepsilon_2(E)$ goes to zero. When the E photon energy is less than the bandgap energy, Eg, $\varepsilon_2(E)$ is zero. The real part of the dielectric function $\varepsilon_1(E)$ can be obtained from $\varepsilon_2(E)$ through the Kramers–Kronig relation.

During the following optical modelling, we used the determined complex refractive indices (and complex dielectric functions) of the pure WO_3 and MoO_3 using the Tauc-Lorentz oscillator model, see Fig. 2. Finding the best match between the model and the experiment is typically achieved through regression analysis. An estimator, like the Mean Squared Error (MSE), is used to quantify the difference between curves.

First, we performed single-target experiments to assess the deposition rate dependence on the power and on the distance from the target. (This way, we determined the angle dependence of "the material stream".) We used 1.5, 1, and 0.75 kW powers. The layer deposition rate is non-linear: double power results in 7 times higher rate in the case of WO_3. We adjusted the used powers for the "double-target" experiments because of the different "walking" speeds and distances.

Double-target samples

1 Targets in closer position

The first (combinatorial) experiment was performed in the „targets in closer position" (Fig. 1 a) The power of the W-target was 0.75 kW, the power of the Mo-target was 1.5 kW. 300 walking cycles were applied with 5 cm/sec walking speed. (We can calculate ~ 1 nm „sublayer thickness" around the center part where the 50 % mixture is expected.) We used a 2-Tauc-Lorentz-oscillator optical model: W-

substrate/interface-layer/T-L(WO₃)+T-L(MoO₃)-mixed-layer/surface-roughness-layer. (This model layer is better for atomic mixture.) 5 fitted parameters were used: the layer thicknesses and the 2 Amplitudes (oscillator strengths). The basic parameters (the Broadenings, the Peak positions and the Bandgap Energies) of the clean materials were determined from the measurements at near the edges of the samples.

Fig. 3 shows the resulted maps (with the schematic optical model): Thickness-map and two Amplitude-maps (T-L(WO₃)–map and T-L(MoO₃)–map) One can see that the composition (Amplitudes) change from 0 % to 100 % in the middle 10-15 cm interval. The composition at the different lateral positions were checked by RBS measurements, too, (see Fig. 4 and 5) which shows good agreement between the results of the two methods.
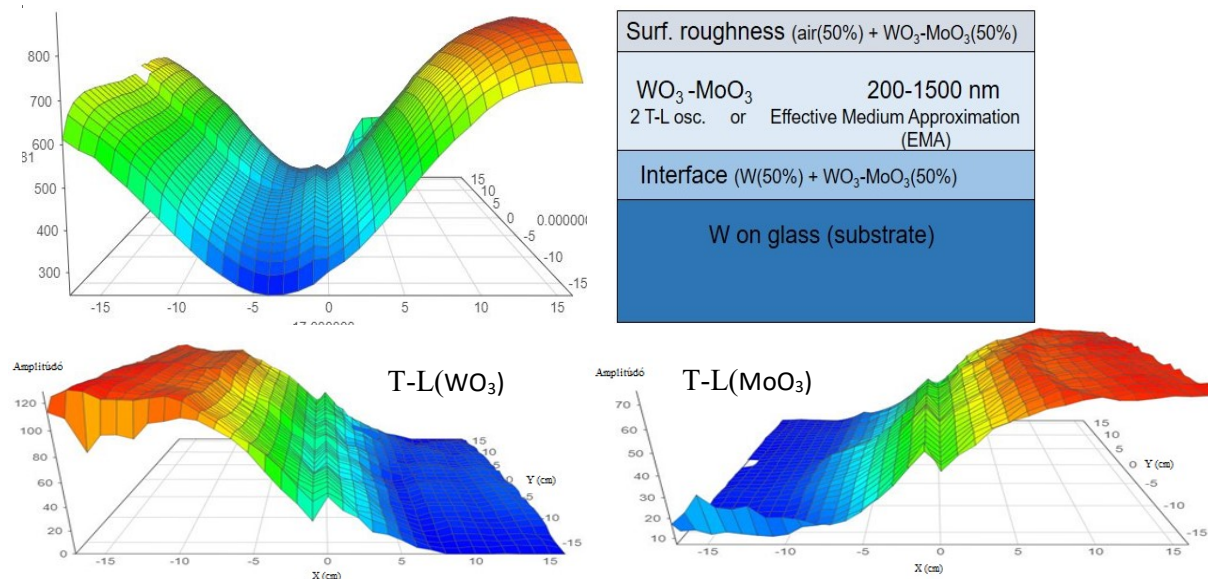
Fig.3 Thickness-map and the schematic optical model (a) Amplitude-of-T-L(WO₃)–map (b) Amplitude-of-T-L(MoO₃)–map (c) (The wrinkles at the centre lines are artefacts caused by the manual "rotation" during the SE measurement.)
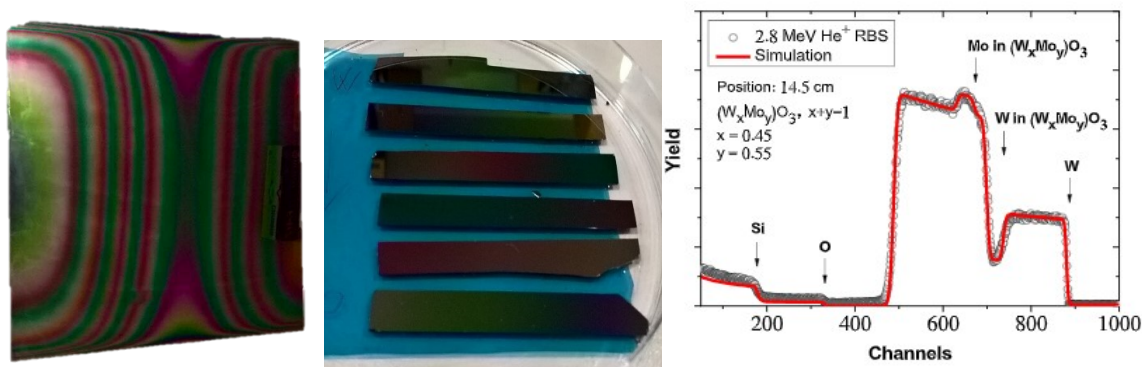
Fig. 4 Photograph of one sample (left) Photograph of the Si-probes which were placed at the centre line of some samples for RBS and XRD (centre) One Rutherford Backscattering Spectrometry example near the centre position. We used the RBX-code [10] to simulate the RBS-spectra.
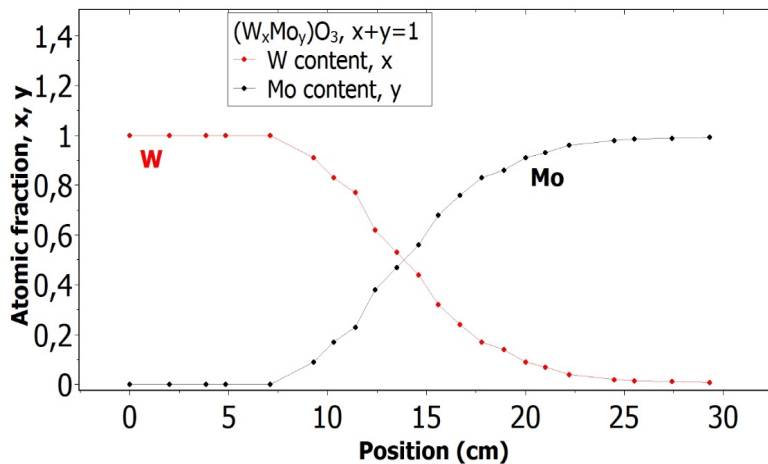
Fig. 5 Composition-map along a line by Rutherford Backscattering Spectrometry

2 Atomic (or „molecular") mixture vs „superlattice"

We prepared two different samples in the „targets in distant" position (Fig. 1 b). The difference was the walking speed (and the number of the walking cycles): one „Fast" (walking speed: 25 cm/sec) and one „Slow" (walking speed: 1 cm/sec) sample. The different speed results in different „sublayer thickness": ~ 0.5 nm for the „Fast" sample and 3-5 nm for the „Slow" sample, calculating from the final thicknesses and the number of the walking cycles around the center part where the 50-50 % mixture is expected. We used two types of optical models: the 2-T-L-oscillator model and the Effective medium approximation (EMA [12]) model (see Fig. 3, upper right) Finding the best match (see Fig. 7 and 9) between the model and the experiment is typically achieved through regression. An estimator, like the Mean Squared Error (MSE), is used to quantify the difference between curves. We can choose between the optical models seeing the MSE-maps: better the model if the MSE values are significantly lower at the relevant (around 50-50 % composition) positions (see Fig. 6 and 8).

2.1 "Fast" sample, 25 cm/sec walking – ~ 0.5 nm „sublayer thickness"

The thickness of the layer around the center part is app. 700 nm. We can calculate a „sublayer thickness" ~ 0.5 nm for this „Fast" sample from the number of the walking cycles (1500) and we can consider it an atomic mixture. Thickness-maps (Fig. 6, upper) show nearly the same results for both optical models. The Amplitude-of-T-L(only WO_3)–map and the EMA(volume percent of WO_3)–map (Fig. 6, middle) and MSE-maps (Fig. 6, lower) show similar tendencies, however the 2-T-L-oscillator model shows significantly lower MSE values against the Effective Medium Approximation model, see the Fig. 10 where the MSE(EMA) – MSE(2 T-L) values are shown. The significantly positive values around the center part (especially around the 50-50 % ratio) show that the 2-T-L-oscillator model is better for this type (atomic mixture) of layer structure. The measured and fitted example spectra on Fig. 7 show that the 2-T-L model is better especially under the 450 nm wavelength region where the light absorbtion is significant.
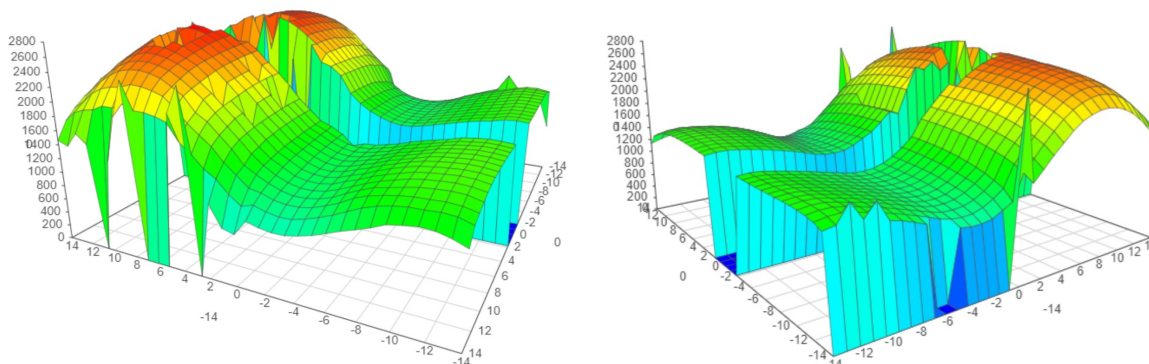
Fig. 6 Thickness-maps (upper), Amplitude-of-T-L(only WO₃)–map and EMA(WO₃)–map (middle) and MSE-maps (lower) using the 2-T-L-oscillator model (left column) and the Effective medium approximation model (The "gaps" around the centre line are due to the Si-probes.)

Fig. 7 Measured and fitted spectra at one sample point: 2-T-L-oscillator-model (left, Fit error (MSE) = 30.4, Thickness = 1159.6 ± 2.9 nm, Amp1 = 39.2 ± 1.1, Amp2 = 26.7 ± 0.4) and Effektive medium approximation model (right, Fit error (MSE) = 40.1, Thickness = 1081.7 ± 0.1 nm, EMA % (Mat 2) = 41.8 ± 0.8)

2.2 "Slow" sample, 1 cm/sec walking – 3-5 nm sublayer thickness

The thickness of the layer around the center part is app. 300 nm. We can calculate a „sublayer thickness" ~ 4 nm for this „Slow" sample from the number of the walking cycles (70) and we can consider it as a „superlattice". (We can say it superlattice only at 50-50 %, otherwise we can call it superlattice-type.) Thickness-maps (Fig. 8, upper) show nearly the same results for both optical models. The Amplitude-of-T-L(only WO₃)–map and the EMA(volume percent of WO₃)–map (Fig. 8, middle) and MSE-maps (Fig. 8, lower) show similar tendencies, however the Effective Medium Approximation model shows significantly lower MSE values against the 2-T-L-oscillator model, see the Fig. 10 where the MSE(EMA) – MSE(2 T-L) values are shown. The significantly negative values around the center part (especially around the 50-50 % ratio) show that the Effective Medium Approximation oscillator model is better for this type („superlattice") of layer structure. The measured and fitted example spectra on Fig. 9 show that the Effective Medium Approximation model is better with an 1.3 % precision of the composition (volume fraction) parameter.
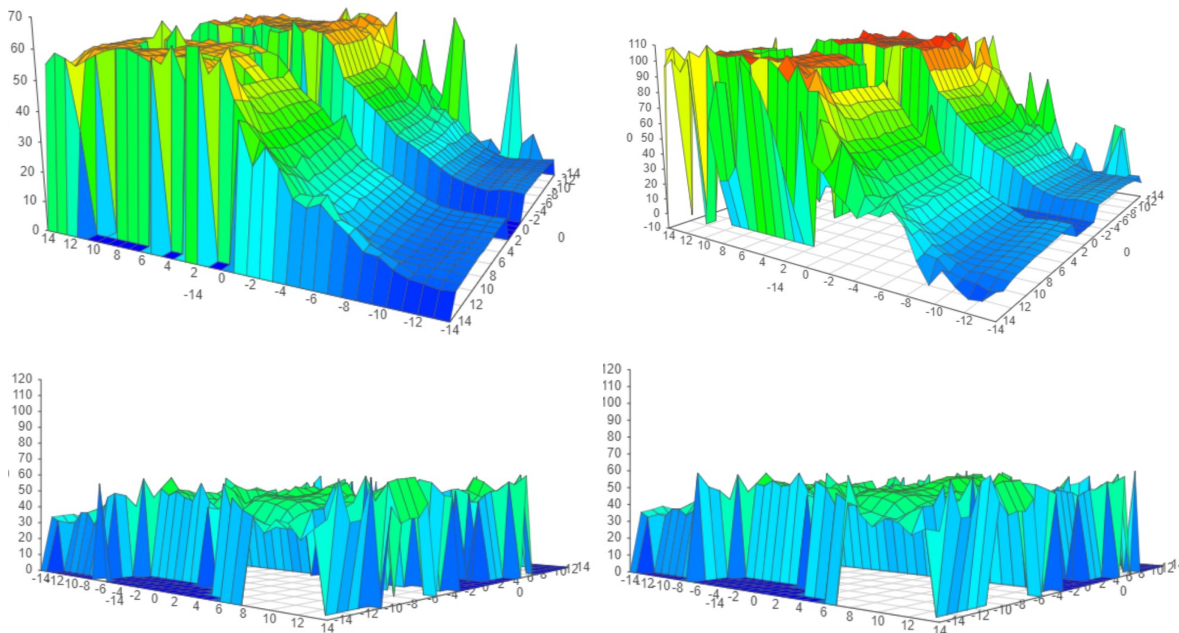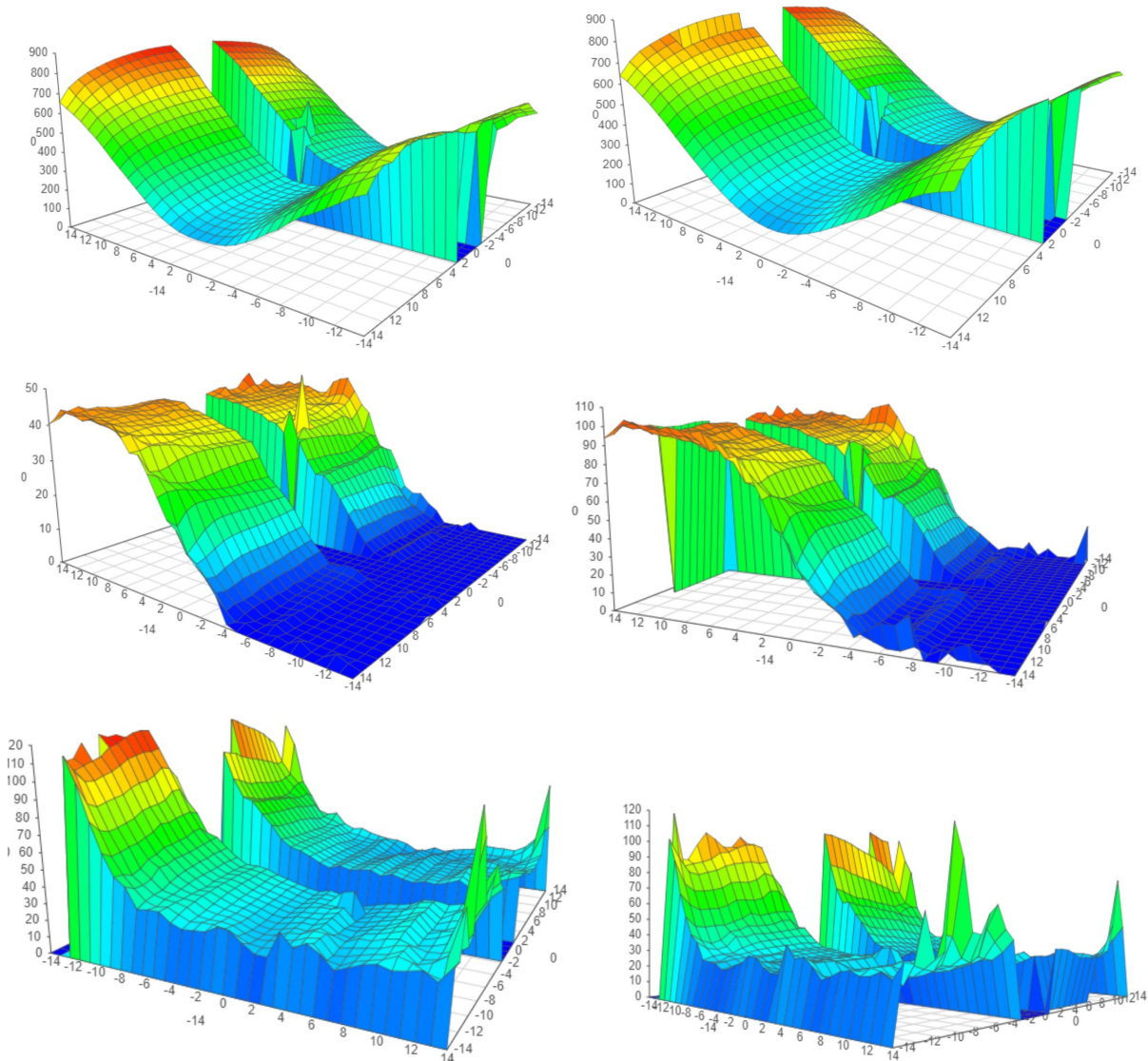

Fig. 8 Thickness-maps (upper), Amplitude-of-T-L(WO₃)–map and EMA(MoO₃)–map (middle) and MSE-maps (lower) using the 2-T-L-oscillator model (left column) and the Effective medium approximation model (The "gaps" around the centre line are due to the Si-probes.)
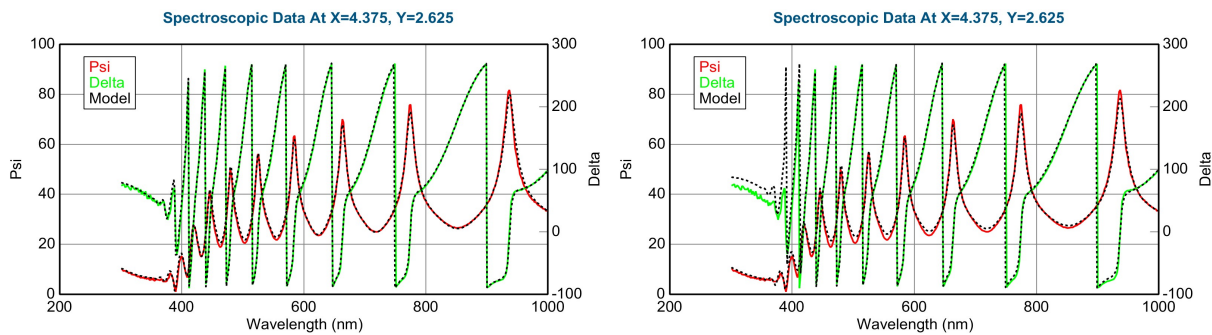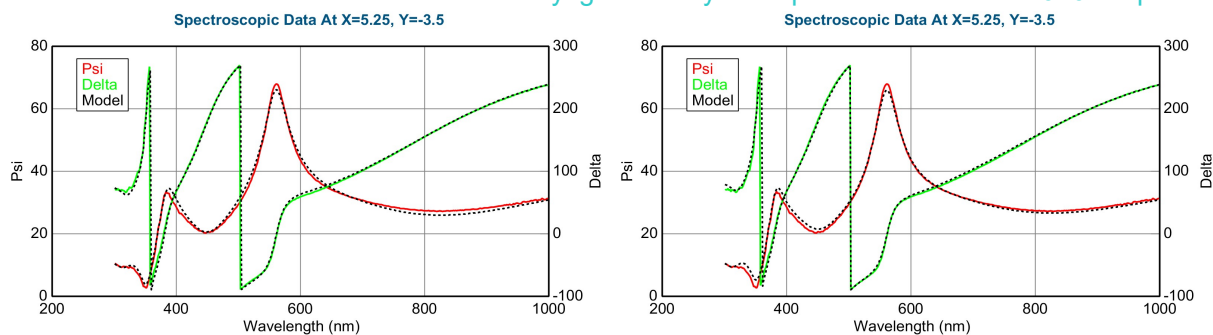
Fig. 9 Measured and fitted spectra at one sample point: 2-T-L-oscillator-model (left, Fit error (MSE) = 29.2, Thickness = 230.4 ± 0.8 nm, Amp1 = 58.0 ± 1.5, Amp2 = 11.4 ± 0.7) and Effektive medium approximation model (right, Fit error (MSE) = 24.8, Thickness = 218.0 ± 0.1 nm, EMA % (Mat 2) = 28.5 ± 1.3)
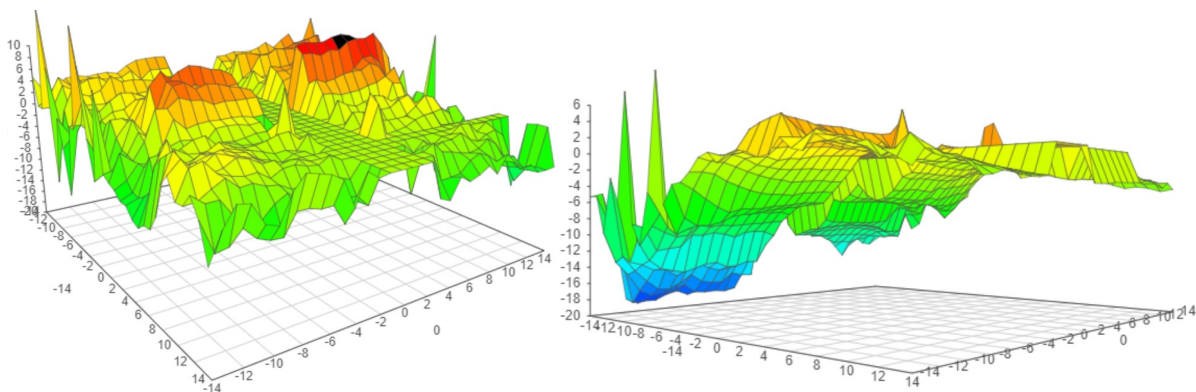
Fig. 10 The MSE(EMA) – MSE(2 T-L) map shows that the 2-T-L-oscillator model is better for the "fast", atomic mixture sample (left), while the Effective Medium Approximation model is better (lower MSE) for "slow", sublayer-type sample (right), especially around the 50-50 % ratio (central) region. (The "gap" (with 0 values) around the centre line are due to the Si-probes.)

Conclusion: We can produce combinatorial samples on large scale in a magnetron sputtering system. These samples can be mapped (thickness and composition maps, too) by fast and non-destructive manner by Spectroscopic Ellipsometry. We can choose between appropriate optical models (2-Tauc-Lorentz-oscillator model versus the Bruggeman Effective Medium Approximation, BEMA) depending on the process parameters. One can conclude that if you have more than one „molecular layer" in the „sublayers" you can use BEMA.

References

[1] C. G. Granqvist, Handbook of Inorganic Electrochromic Materials (Elsevier, Amsterdam, 1995) P. P. Gonzalez-Borrero, F. Sato, A.N. Medina, M.L. Baesso and A.C. Bento: Applied Physics Letters. Vol. 96, 061909 (2010); doi: http://dx.doi.org/10.1063/1.3313945

[2] J. Livage and D. Ganguli: Solar Energy Materials & Solar Cells. Vol. 68 (2001), p. 365-381

[3] C.S. Hsu, C.C. Chan, H.T. Huang, C.H Peng and W.C Hsu: Thin Solid Films. Vol. 516 (2008), p. 4839-4844

[4] S.Y. Lin, C.M. Wang, K.S. Kao, Y.C. Chen and C.C. Liu: Journal of Sol Gel Science and Technology. Vol. 53 (2010), p. 51

[5] V. Madhavi, Jeevan Kumar Padarti, Paruchuri Kondaiah, Owais Hussain, S. Uthanna, Ionics vol. 20(12) (2014) 1737-1745

[6] T. Ivanova, K.A. Gesheva, M. Kalitzova, F. Hamelmann, F. Luekermann and U. Heinzmann: Journal of Optoelectronics and Advanced Materials. Vol. 11 (2009), p. 1513-1516

[7] A. Novinrooz, M. Sharbatdaran and H. Noorkojouri: Central European Science Journals (2005), p. 456-466

[8] Ch.Prameelaand, K.Srinivasarao; International Journal of Applied Engineering vol. 10(4) (2015) pp. 9865-9875

[9] https://www.jawoollam.com/products/m-2000-ellipsometer

[10] E. Kótai, Computer Methods for Analysis and Simulation of RBS and ERDA spectra, Nucl. Instr. Meth. B 85 (1994) 588 - 596.

[11] G.E. Jellison, Jr. and F.A. Modine, Appl. Phys. Lett. 69, 371 (1996), Erratum, Appl. Phys. Lett. 69, 2137 (1996)

[12] D. A. G. Bruggeman, Ann. Physik (Leipzig) 24, 636 (1935)

About the self-assembled III-V-based nano-structures
or mysteries of droplet epitaxy

Ákos Nemcsics

Institute of Microelectronics and Technology, Óbuda University, 1084 Budapest, Tavaszmező utca 17., Hungary; nemcsics.akos@kvk.uni-obuda.hu.

Introduction: Applications (QD – solar cell, QD – computing etc.) ; Material (GaAs and other III-V materials) ; Technology (epitaxy, MBE, RHEED, equipment); RHEED tracking and image processing; Droplet epitaxy (fundamentals); Kinetics of QD growth; growth of nano-structure ensembles; technological support (technological data processing for support of technology)

Keywords: droplet epitaxy, GaAs and related materials, MBE, RHEED, quantum dot

Introduction.

Applications (QD solar cells, QD computing).
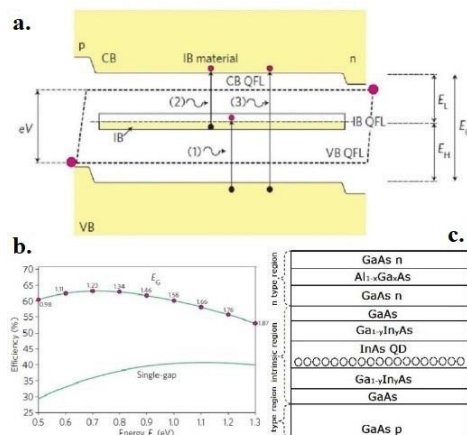
Fig. 1. *Electronic structure of a QD solar cell. The figure originate from Ref. [1]. Further literature herein.*
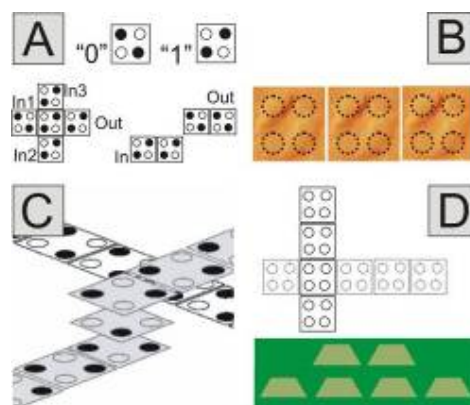
Fig. 2. *QCA realized by droplet epitaxially grown QD ensembles. The figure originate from Ref. [2]. Further literature herein.*

Technology

Droplet epitaxial fundamentals and the equipment
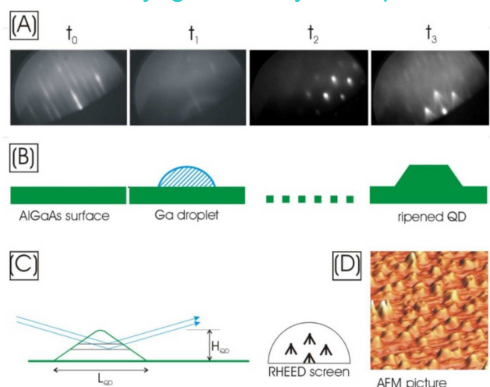
Fig. 3. *QD growth by droplet epitaxy. The figure originate from Ref. [3]. Further literature herein*
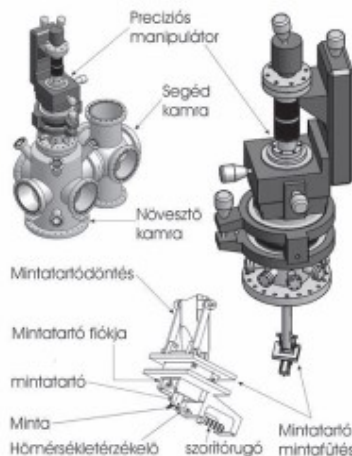
Fig. 4. *Main parts of self-developed MBE equipment. The figure originate from Ref. [4]. Further literature herein.*

RHEED tracking

Fig. 5. *RHEED patterns observed step by step manner during the evolution of the quantum objects and the AFM picture of the ripened structure. The upper and lower parts concern QD and QR, respectively. The density of QDs and QRs are 3.6×10^{10} and 1.5×10^9 cm^{-2}.[5]*
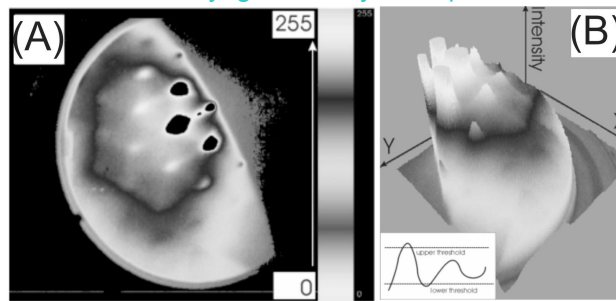
Fig. 6. *RHEED picture is displayed after image processing. The intensity distribution after the upper and lower cutting in 2D (see insert). The same in 3D. It makes the intensity around the evolved shapes easier to observe.[6]*

Faceting of nano-structures
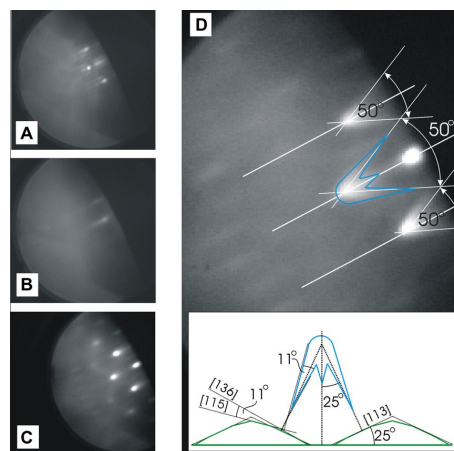
Fig. 7. *The change of the RHEED pattern in different stages of the QD formation. (A) The RHEED pattern of the initial AlGaAs surface. (B) The RHEED pattern after the Ga deposition. (C) The RHEED pattern after the opening of the arsenic cell; the dotted pattern represents monocrystalline transmission character (see text). (D) The appearance of the chevron-tails after the annealing stage and (insert) its explanation. The chevron-tails appear only in later stage of the crystallization, when the shape of the nanostructurebecomes characteristic. These chevron-tails are not sharp but rather broadened [7].*
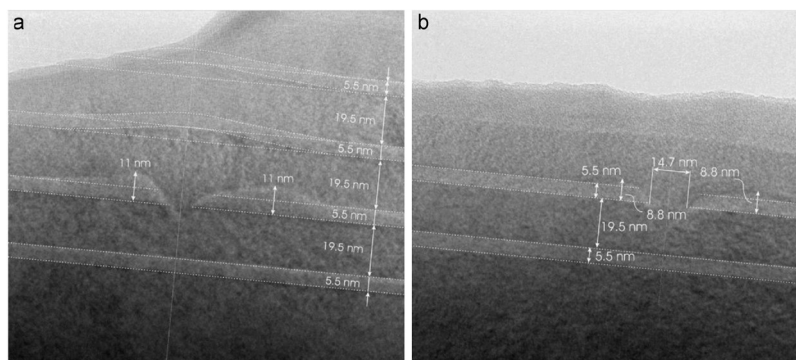
Fig. 8. *(a) TEM picture of an inverted NH-QD and its environment. The lines serve as guides to eye to recognize the structures. The structures consists of a AlAs (5.5 nm)/AlGaAs (19.5 nm) superlattice with a NH-QD in the center. (b) Second NH-QD*

Growth kinetics and nano-positioning
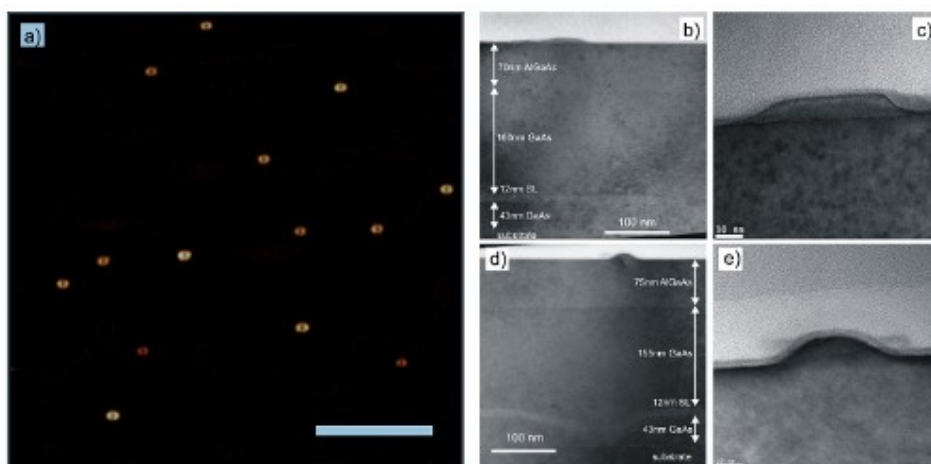
Fig. 9. *Panel a: 2_2_m2 AFM scan of the surface of sample A. Panels b to e show cross sectional HR-TEM image of the sample. Panels c and e show larger magni_cation of the same nanostructures in panels b and d, respectively.[9]*
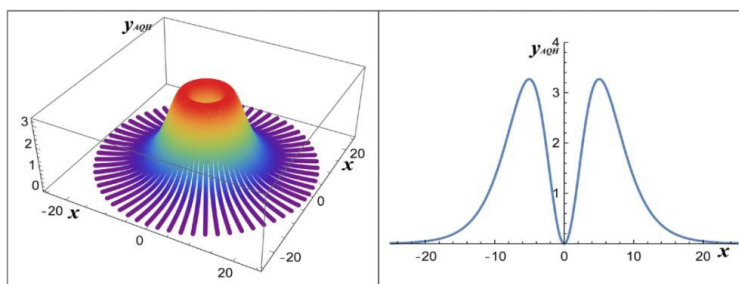
Fig. 10. *3D and the 2D cross section of a typical QR.*

References

[1] Antal Ürmös, Zoltán Farkas, Márk Farkas, Tamás Sándor, László T. Kóczy, Ákos Nemcsics: Application of Self-Organizing Maps for Technological Support of Droplet Epitaxy; Acta Polytechnica Hungarica; 14 : 4 pp. 207-224. , 18 p. (2017).

[2] Ákos Nemcsics: Droplet Epitaxy as a Tool for the QD-Based Circuit Realization; InTech; https://www.intechopen.com/books/nonmagnetic-and-magnetic-quantum-dots/droplet-epitaxy-as-a-tool-for-the-qd-based-circuit-realization

[3] Ákos Nemcsics: Quantum Dots Prepared by Droplet Epitaxial Method; InTech; https://www.intechopen.com/books/quantum-dots-theory-and-applications/quantum-dots-prepared-by-droplet-epitaxial-method

[4] Ákos Nemcsics, stván Réti, Gusztáv V. Tényi, Péter Kucsera, László Tóth, Péter Harmat, Mieville Amadou,Márton Csutorás, Béla Kupás-Deák, Tamás Sándor,Judit Bozsik::Technical Conditions for the Formation of Molecular-Bem-Epitaxial Nanostructures; GÉP, LXI. évfolyam, 2010.

[5] A. Nemcsics, Ch. Heyn, A. Stemmann, A. Schramm, H.Welsch,W. Hansen: The RHEED tracking of the droplet epitaxial grown quantum dot and ring structures; Mat. Sci. Eng. B 165 (2009) 118–121

[6] Péter Kucsera, Tamás Sándor, Gusztáv Varga Tényi, Márton Csutorás, Gergely Bátori, Béla Kupás-Deák, István Réti, Antal Ürmös, Ákos Nemcsics: Nanostructure Growth Supported by In Situ RHEED Evaluation; Materials Science Forum Vol. 885, (2016) pp 234-238

[7] Ákos Nemcsics, Lajos Tóth, László Dobos, Andrea Stemmann: Facetting of the self-assembled droplet epitaxial GaAs quantum dot; Microel. Reliab. 51 (2011) 927.

[8] Á. Nemcsics, Ch. Heyn, L. Tóth, L. Dobos, A. Stemmann, W. Hansen: Cross-sectional transmission electron microscopy of GaAs quantum dots fabricated by filling of droplet-etched nanoholes; Journal of Crystal Growth 335 (2011) 58–61

[9] Bietti S, Basset FB, Scarpellini D, Fedorov A, Ballabio A, Esposito L, Elborg M, Kuroda T, Nemcsics Ákos, Toth L, Manzoni C, Vozzi C, Sanguinetti S: Ga metal nanoparticle-GaAs quantum molecule complexes for terahertz generation; Nanotechnology 29 : 36 Paper: 365602 , 8 p. (2018)

[10] J. Takács, Á. Nemcsics: QD to NH; Mathematical Modelling of Nano-structure Formations; Scientific Review 2413-8835 Vol. 4, Issue. 9, (2018) pp: 74-79.

Biosensing in the ultraviolet wavelength range by Kretschmann-Raether ellipsometry

Benjamin Kalas[1,2], Kárpát Ferencz[3,4], András Saftics[1], Zsolt Czigány[1], Miklós Fried[1], Péter Petrik[1]

[1]*Institute for Technical Physics and Materials Science, Centre for Energy Research, Konkoly-Thege Rd. 29-33, 1121 Budapest, Hungary*
[2]*Doctoral School of Physics, Faculty of Science, University of Pecs*
[3]*Institute for Solid State Physics and Optics, Wigner Research Centre for Physics, Konkoly-Thege Rd. 29-33, 1121 Budapest, Hungary*
[4]*Optilab Ltd., Sulyok Str. 2, 1031 Budapest, Hungary*

Optical biosensors are sensitive, non-destructive, label-free and capable of quick in-situ characterization. Among the many types of optical sensors those utilizing the surface plasmon resonance (SPR) are one of the most popular. Biological processes are usually accompanied with a change of dielectric function in the layer or at the interface, and they can therefore be followed by in-situ high-sensitivity optical characterization techniques. The SPR method usually utilizes the Kretschmann-Raether configuration, in which there is a metal layer at the interface which is illuminated from the media of the higher refractive index. The features of the plasmons excited in the metal layer can be analyzed by detection at changing angle of incidence, wavelength, or both. SPR sensors usually measure the reflected intensity, but with ellipsometry the difference between the r_p and r_s polarizations can be measured also in term of phase, where r_p and r_s denote the complex reflection coefficients of light polarized parallel and perpendicular to the plane of incidence, respectively.

In this work a Bragg multilayer structure (Fig. 1) was designed utilizing materials of SiO_2 and ZrO_2 that creates an interference feature in the ultraviolet wavelength range. The target wavelength was 270 nm, at which most proteins have an absorption peak. The peak position can be adjusted by the angle of incidence, but also by the layer structure and the thicknesses, which opens an opportunity to use combinatory [2] in the Kretschmann-Raether configuration. The width of the peak at half maximum is as small as 3 nm. Using one or multiple resonant peaks in the spectrum helps to increase the selectivity of the sensor, although the sharp feature is a challenge in terms of spectral resolution of the monochromator. It might cause depolarization, such as the focusing of the beam. Focusing is on the other hand an enabler for combinatorial applications, in which the lateral resolution can be identified as the resolution of the composition. The peak position can be adapted to specific materials and tasks. Compared with the traditional plasmonics, the position, the width or even the number of peaks can be changed. All these features are important when targeting a good selectivity, besides the sensitivity, which can be achieved even by a purely spectroscopic approach, i.e. without changing the angle or using any moving parts in the configuration. The demonstrated sensitivity was $6.55 \cdot 10^{-6}$ and 10.4 pg/mm^2 for the refractive index and for the surface mass density.
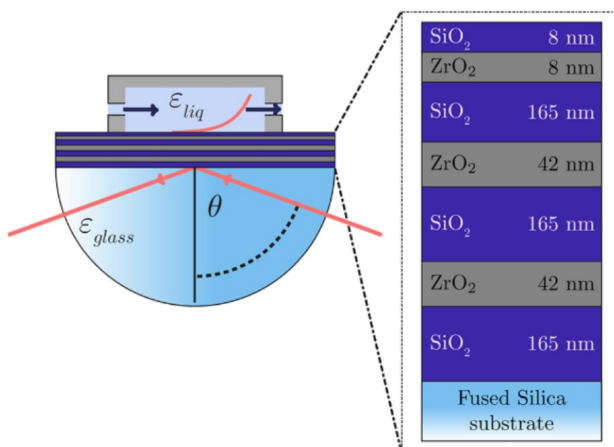
Figure 1: Kretschmann-Raether ellipsometry using multilayer optimized for enhanced sensitivity at the wavelength of 270 nm. Most proteins have and absorption peak at this wavelength.

Keywords: bioellipsometry, biosensing, optical characterization, optical properties of proteins

References

[1] B. Kalas, K. Ferencz, A. Saftics, Z. Czigany, M. Fried, P. Petrik, Bloch surface waves biosensing in the ultraviolet wavelength range – Bragg structure design for investigating protein adsorption by in situ Kretschmann-Raether ellipsometry, Applied Surface Science. 536 (2021) 147869. https://doi.org/10.1016/j.apsusc.2020.147869.

[2] B. Kalas, Z. Zolnai, G. Sáfrán, M. Serényi, E. Agocs, T. Lohner, A. Nemeth, N.Q. Khánh, M. Fried, P. Petrik, Micro-combinatorial sampling of the optical properties of hydrogenated amorphous $Si_{1-x}Ge_x$ for the entire range of compositions towards a database for optoelectronics, Scientific Reports. 10 (2020) 19266. https://doi.org/10.1038/s41598-020-74881-5.

Single-nanoparticle spectroscopy in colloid chemistry

Dániel Péter Szekrényes[1], Szilárd Pothorszky[1], Dániel Zámbó[1], Norbert Nagy[1], Zoltán Hajnal[1], Zoltán Osváth[1], Zsolt Zolnai[1] and András Deák[1*]

[1]Centre for Energy Research, Konkoly-Thege Miklós út 29-33., 1121 Budapest, Hungary

In this work we present our latest results on the possibilities to study ligand exchange and self-assembly of gold nanoparticles by optical methods, with a special focus on engineering colloidal interaction between the particles. We employ the chemical interface damping (CID) increase related scattering peak broadening of individual gold nanorods due to thiol-molecule binding to study the ligand exchange at the rods' surface. We show that the interaction between the already adsorbed and adsorbing ligands is especially important when both ligands are charged. We also highlight how ligand-exchange can be used for the controlled preparation of gold nanoparticle dimers. By analyzing the plasmon coupling upon dimer formation (plasmon ruler, deconvolution of the coupled spectrum, optical simulations), one can obtain information on the spatial arrangement of the dimers, which is largely determined by the surface grafted molecules.

Keywords: plasmonics, scattering microspectroscopy, surface-modification, self-assembly

Introduction

Noble metal nanoparticles offer a unique opportunity to study physicochemical processes at a length scale that is highly relevant for colloid science. This feature stems from the localized plasmon modes these particles can support when the conduction band electron are forced to collective oscillation upon illumination with light. The few tens of nanometres spatial extent of the optical near-field that develops as a result of this collective oscillation falls in the range typically of interest in colloid science. The associated sensitivity of the scattering spectrum of these particles on the properties of the embedding medium makes them an ideal model system to follow ligand-exchange or self-assembly processes even down to the individual nanoparticle level. This latter is especially useful as it allows – when supplemented with other high resolution investigation methods like atomic force o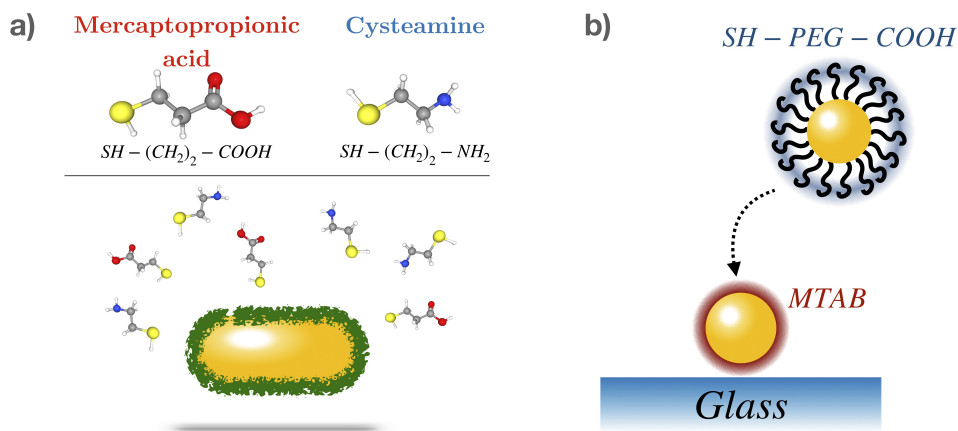r electron microscopy - a more rigorous interpretation of the physical and chemical processes and hence a deeper insight into phenomena that often determine the behaviour of nanosized systems.

The motivation of the current work is twofold (Scheme 1). First, recent literature results show that the binding of thiols to gold nanoparticles induces plasmon peak-broadening due to increasing CID.[1] We exploit this effect to investigate how single nanoparticle scattering spectroscopy can be used to study in detail ligand exchange reactions at the nanoparticles' surface. Second, we use this techniques to asses in-situ, in aqueous environment the effective stabilizing effect of PEG molecules, that are the prototypical molecules in nanomedicine to render the body-introduced agents 'invisible' (stealth function). For this, we design nanoparticles that form dimers – one of them having PEG molecules grafted on the surface. The nanoparticle dimers are formed in a liquid cell and studied in-situ by microspectroscopy. Upon dimer formation, the plasmon coupling can be used to extract the average equilibrium distance between the particles (plasmon ruler). By complementing the measurements with detailed colloid interaction energy calculations, the effective influence of the PEG molecules on the particle stability can be derived.

a) **Mercaptopropionic acid**   **Cysteamine**

$SH - (CH_2)_2 - COOH$ $SH - (CH_2)_2 - NH_2$

b) $SH - PEG - COOH$

MTAB

Glass

Scheme 1: a) Ligand exchange of CTAB (green) using two, oppositely charged small thiol molecules cause change in the particles optical spectrum that can reveal the details of the ligand exchange procedure. b) Assembly of oppositely charged dimers and the resulting optical changes provide information about the relevant colloidal interactions and the role of PEG.

Experimental

The nanospheres and nanorods have been synthesized according to already published protocols.[2,3] The ligand exchange process of the nanorods' original CTAB capping layer was studied using different small-molecule thiols (cysteamine, mercaptopropionic acid) and has been followed on the ensemble level by Vis-spectroscopy and dynamic light scattering. For the single-particle experiments the nanoparticles have been first deposited on glass substrate and integrated in a liquid cell. The cell allowed changing the solution composition conveniently using a peristaltic pump. The scattering spectra of individual nanoparticles was measured on a laboratory developed, dark-field optical microscope based microspectroscopy setup.[4]

Results

CTAB itself has an interesting effect on the resonance peak of the nanorods. Recent papers state that the CTAB stabilizes silver on the rods' surface and when the CTAB concentration is varied in the bulk, this combined effect is responsible for the observed damping changes.[5] We observe in contrast in the peak positions and damping values even when *only* the CTAB concentration is varied and no silver is added to the system (Figure 1).[4] This indicated that that – besides the silver present directly at the interface – the negatively charged counter ions might also have a significant influence on CID, which will be the subject of our investigation in an upcoming work.
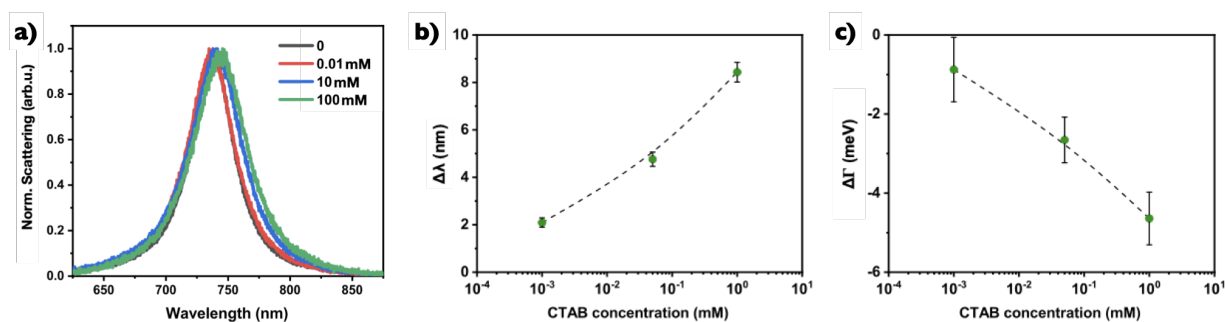
Figure 1: a) Scattering peak of a selected, individual gold nanorod at different, increasing CTAB concentrations. The wavelength (b) and damping (c) changes derived from fitting the oscillator model to the measured peaks.[4]

When the nanorods became in contact with the thiols, there is a significant difference in the damping and position change of the resonance peak. While the positively charged cysteamine was found to effectively replace the similarly positive charged CTAB, a self-limiting ligand-exchange was found for the negatively charges mercaptopropionic acid. This underlines the central importance of intermolecular interaction during ligand during the ligand exchange process.[4]

For the surface modified spherical nanoparticles, the equilibrium particle-particle distance dependent optical changes of the scattering spectrum as a result of plasmon coupling is usually represented by the so called plasmon ruler. This indicates an exponential like redshift of a coupled mode as the particles approach each

other. For our work we derived a theoretical plasmon ruler by simulating the scattering spectra of dimer nanospheres using the boundary element approach.[6] During the retarded simulations the particle size range of interest, the presence of a substrate and the limited collection angle of our experimental setup were all taken into account. Especially for larger particles, our results show some deviation from the prediction of the classical plasmon ruler equation.[7]

$$\lambda = \lambda_0 + \lambda_0 A e^{\frac{-x}{\tau D}} \qquad \lambda = a(1 - e^{-bx^c})$$
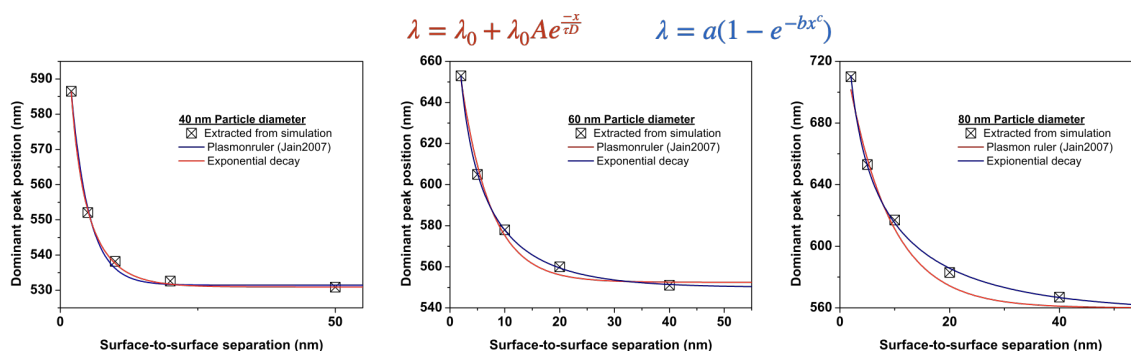
Figure 2: Simulated peak-position of a nanoparticle dimer as a function of gap size.

Figure 3 shows the experimental realization of a nanoparticle dimer with the associated spectral changes. It has to be emphasized that the optical spectra are recorded *in-situ* in the liquid cell upon dimer formation, while the inset shows the ex-situ recorded correlative SEM image. Using the plasmon ruler of given particle size, a gap size of 3.4 nm can be derived, which is reasonable for the given PEG size (3000 Da). Further work will focus on the quantification of the equilibrium particle separations under varying conditions (mainly pH and ionic strength) that affect the strength of the interaction potential and will compare the result to colloidal interaction calculations.
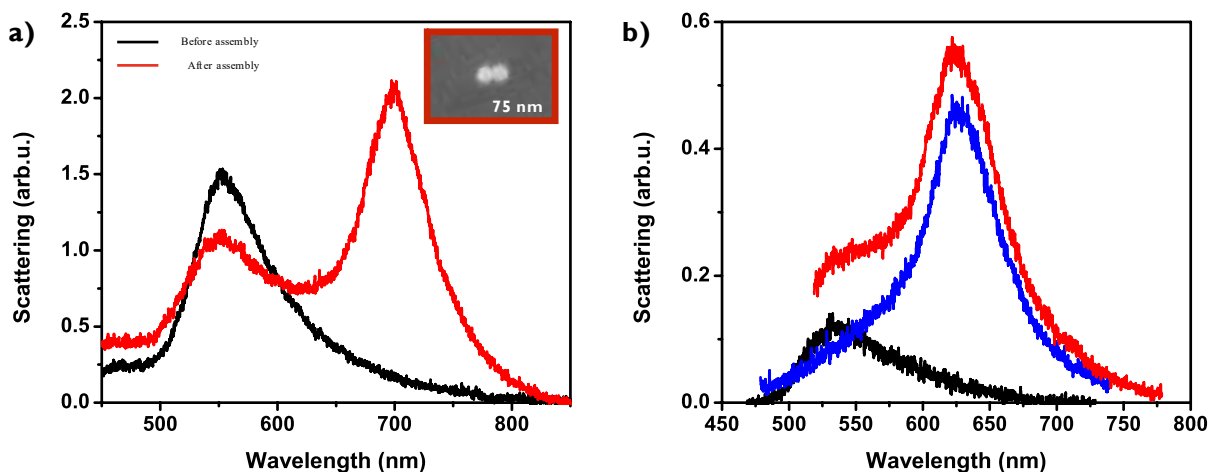
Figure 3: Scattering spectra of an individual scatterer measured before and after dimer formation for 75 nm (a) and 60 nm (b) diameter particles.

Acknowledgement

References

(1)   Foerster, B.; Spata, V. A.; Carter, E. A.; Sönnichsen, C.; Link, S. Plasmon Damping Depends on the Chemical Nature of the Nanoparticle Interface. *Sci. Adv.* **2019**, *5* (3), eaav0704. https://doi.org/10.1126/sciadv.aav0704.

(2)   Hanske, C.; González-Rubio, G.; Hamon, C.; Formentín, P.; Modin, E.; Chuvilin, A.; Guerrero-Martínez, A.; Marsal, L. F.; Liz-Marzán, L. M. Large-Scale Plasmonic Pyramidal Supercrystals via Templated Self-Assembly of Monodisperse Gold Nanospheres. *J. Phys. Chem. C* **2017**, *121* (20), 10899–10906. https://doi.org/10.1021/acs.jpcc.6b12161.

(3)   Ye, X.; Zheng, C.; Chen, J.; Gao, Y.; Murray, C. B. Using Binary Surfactant Mixtures To Simultaneously Improve the Dimensional Tunability and Monodispersity in the Seeded Growth of Gold Nanorods. *Nano Lett.* **2013**, *13* (2), 765–771. https://doi.org/10.1021/nl304478h.

(4)   Szekrényes, D. P.; Kovács, D.; Zolnai, Z.; Deák, A. Chemical Interface Damping as an Indicator for Hexadecyltrimethylammonium Bromide Replacement by Short-Chain Thiols on Gold Nanorods. *J. Phys. Chem. C* **2020**, *124* (36), 19736–19742. https://doi.org/10.1021/acs.jpcc.0c04629.

(5)   Ye, W.; Krüger, K.; Sánchez-Iglesias, A.; García, I.; Jia, X.; Sutter, J.; Celiksoy, S.; Foerster, B.; Liz-Marzán, L. M.; Ahijado-Guzmán, R.; Sönnichsen, C. CTAB Stabilizes Silver on Gold Nanorods. *Chem. Mater.* **2020**, *32* (4), 1650–1656. https://doi.org/10.1021/acs.chemmater.9b05139.

(6)   Waxenegger, J.; Trügler, A.; Hohenester, U. Plasmonics Simulations with the MNPBEM Toolbox: Consideration of Substrates and Layer Structures. *Comput. Phys. Commun.* **2015**, *193*, 138–150. https://doi.org/10.1016/j.cpc.2015.03.023.

(7)   Jain, P. K.; Huang, W.; El-Sayed, M. A. On the Universal Scaling Behavior of the Distance Decay of Plasmon Coupling in Metal Nanoparticle Pairs: A Plasmon Ruler Equation. *Nano Lett.* **2007**, *7* (7), 2080–2088. https://doi.org/10.1021/nl071008a.

Gold-epoxy nanomushroom arrays – fabrication and possible application areas

Attila Bonyár[1*], Tomáš Lednický [2] and Shereen Zangana[1]

[1] *Department of Electronics Technology, Budapest University of Technology and Economics, Budapest H-1111, Hungary*
[2]*CEITEC - Central European Institute of Technology, Brno University of Technology, Brno 612 00, Czech Republic*
*bonyar@ett.bme.hu

Abstract: The fabrication technology and two possible application areas of a gold-epoxy surface nanocomposite are presented. The nanocomposite is made of ordered nanoparticles on top of etched epoxy pillars, forming an array of 'nano-mushrooms'. The presented technology enables the large-scale fabrication of such composites (e.g., with a cm^2 surface area) with control over the size and interparticle distance of the nanoparticles. The possibility to utilize such nanocomposites as label-free biosensors in LSPR (localized surface plasmon resonance) configurations and also as SERS (surface-enhanced Raman spectroscopy) substrates is presented.

Keywords: nanocomposite, plasmonics, LSPRi, SERS

1. Introduction

Recently, the development of plasmonic nanomaterials became one of the focal points of materials science research, due to their unique optical properties, such as their extremely high absorption and scattering efficiency or excellent sensitivity to the dielectric properties of the surrounding medium. Relying on these properties, plasmonic nanostructures offer a large potential for bioanalytical applications, such as LSPRi and SERS as well. Localized surface plasmon resonance imaging (LSPRi) – the utilization of collective electron oscillations, which are incited on the nanoparticles, as sensors – promises the possibility of high throughput biomolecule sensing integrated into miniaturized point-of-care (PoC) devices [1]. Surface-enhanced Raman spectroscopy (SERS) is a promising ultrasensitive method in which the Raman scattering signal strength of molecules, absorbed on the surface of metallic nanoparticles with intensive near-fields, is enhanced with several orders of magnitude [2]. Both techniques require nanoparticles or nanostructures, preferably bound to a surface. Besides, the sensitivity of both methods is depending on the intensity of the plasmon field around the particles, which can be enhanced by utilizing plasmonic coupling between closely packed nanoparticles [3-5].
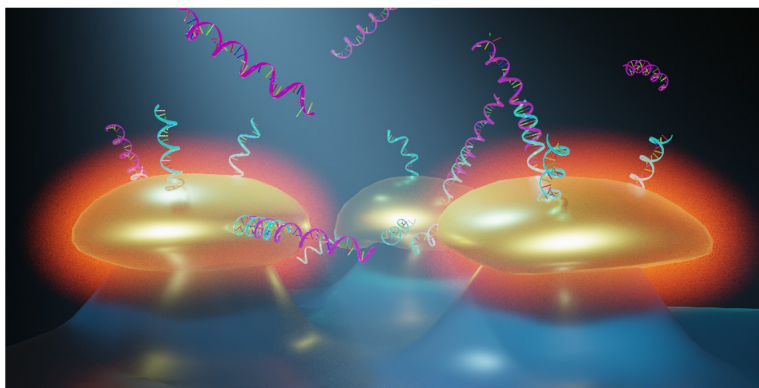

Figure 1. *3D illustration of the fabricated gold-epoxy nanomushroom arrays and their possible use as nucleotide sensors [4].*

In this work, we present a fabrication technology to prepare gold-epoxy surface nanocomposites (nano-mushrooms, as illustrated in Fig.1), where closely packed gold nanoparticles form an array on a large

surface area, with controllable particle size and interparticle distance, which is essential for the optimization of these substrates for LSPR and SERS purposes. The application of these nanocomposites for the label-free detection of DNA fragments with these methods is also demonstrated.

2. Fabrication Technology

The main steps of the fabrication technology are presented in Figure 2. A detailed description of the different steps can be found in our previous works [4,5]. In short, the nanoparticles are synthesized by solid-state dewetting on nanobowled aluminum templates, which are prepared by the selective chemical etching of porous anodic alumina (PAA) grown on an aluminum sheet with controlled anodic oxidation. This flexible fabrication technology provides proper control over the nanoparticle size, shape, and interparticle distance over a large surface area (several cm^2), which enables the fine-tuning and optimization of their plasmonic absorption spectra for LSPR and SERS applications between 535–625 nm. The nanoparticles are transferred to the surface of epoxy substrates, which are subsequently selectively etched [5]. In the examples presented in this paper, samples with a cell size of 110 ± 5 nm, and an average particle diameter of 92 ± 6 nm are used.
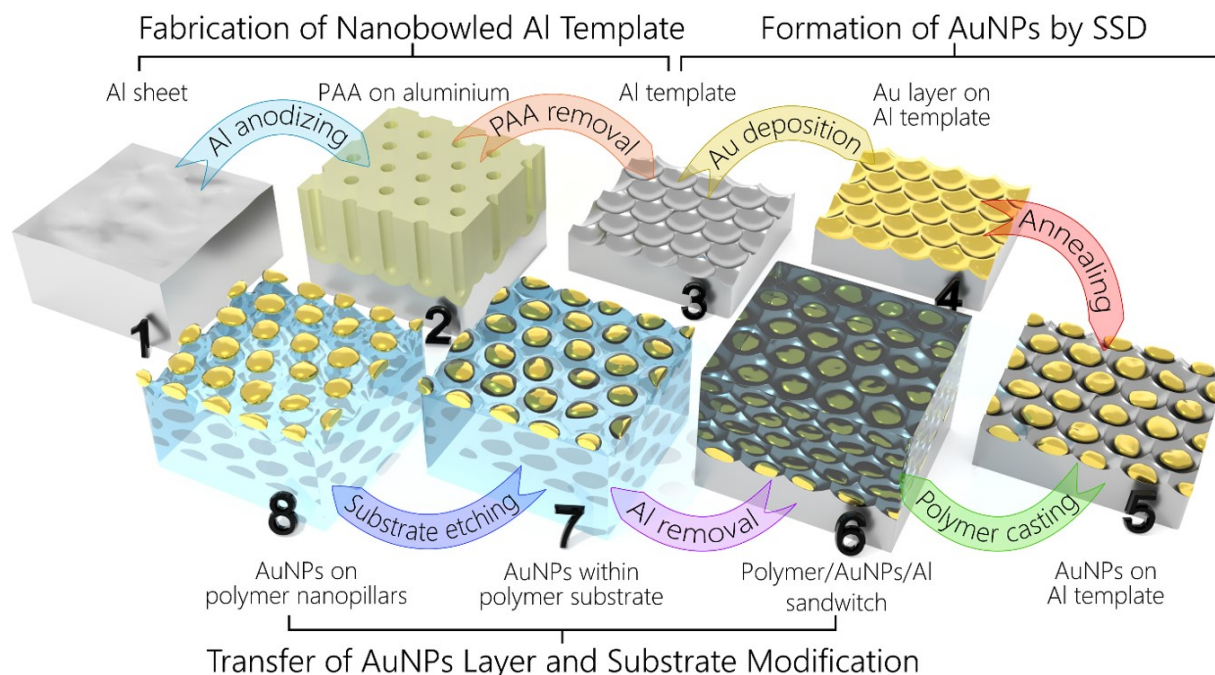
Figure 2. *The main fabrication steps of gold-epoxy nanomushroom array preparation. [4]*

3. LSPR

Optical spectroscopy measurements were performed with an Avantes Avaspec 2048-4DT spectrometer and an Avantes Avalight DHS halogen light source. The bulk refractive index sensitivity of the plasmonic sensors was tested by changing the medium above the samples between air, de-ionized water, and a sucrose dilution series (25 %, 50 %, 75 % and 100% in di water, as shown in Fig. 3.A). The sensor surface was illuminated in a circular area with a diameter of 8 mm and a glass microscope sheet was used to cover the dispersed media on the samples. The obtained RI sensitivity of our sensors was between 85-120 nm/RIU, depending on the fabrication technology [5].
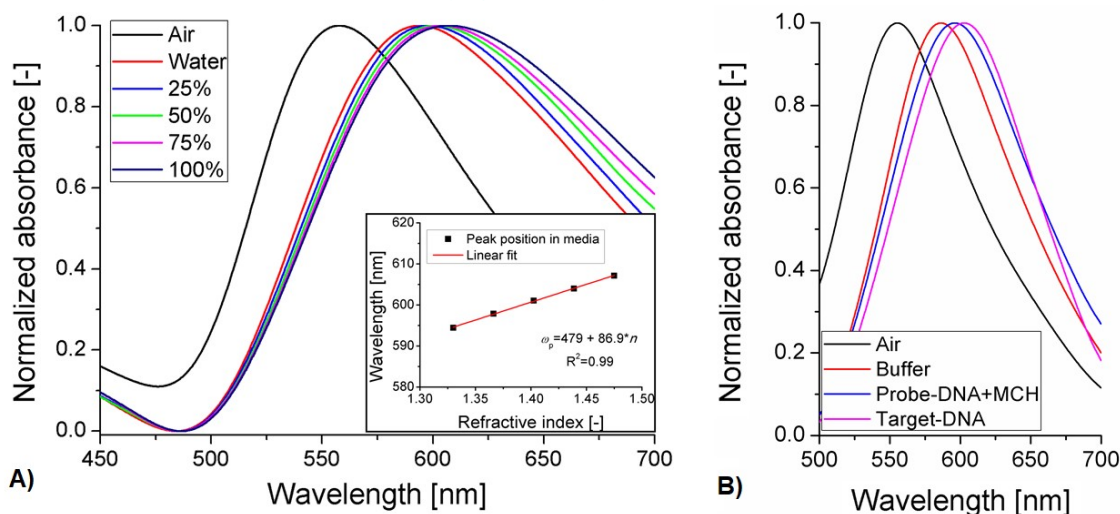
Figure 3. A) LSPR absorbance spectra of a nanocomposite sensor in different calibration media (sucrose solution). Insert: the corresponding peak positions and linear fit. B) The response of the sensor to probe- and target single-stranded DNA, respectively. [5]

Nucleotide sensor tests were performed by using 20 bases long probe- and target-DNA molecules that form a specific sequence from the parasite Giardia lamblia (the β-giardin gene) [6]. We used the same DNA functionalization protocols, which were tested in a previous work [7], including 1) overnight probe immobilization from 1 μM solution; 2) 30 min 6-mercapto-1-hexanol (MCH) treatment after probe immobilization to reduce nonspecific binding of DNA on the gold surface, 3) 2 h binding of target-DNA from a 1 μM solution. As shown in Fig. 3. B), these treatments caused a redshift of 9.4 ± 0.8 nm after probe immobilization and 6.6 ± 0.7 nm after target hybridization. As demonstrated in our paper [5], with these protocols, it was possible to reach a limit of detection around 5 nM for this 20 bp long target DNA.

4. SERS

SERS measurements were performed with a Renishaw InVia Raman spectrometer at 633 nm laser wavelength on a nanocomposite sample with an acquisition time of 10 s. Fig. 4 shows the obtained SERS spectrum of a 20 base pair long ds-DNA bound on the gold NPs. The observed peaks correspond well with Raman bands previously associated with the bases (adenine, cytosine, guanine, and thymine) or the sugar-phosphate backbone (deoxyribose) [8,9].
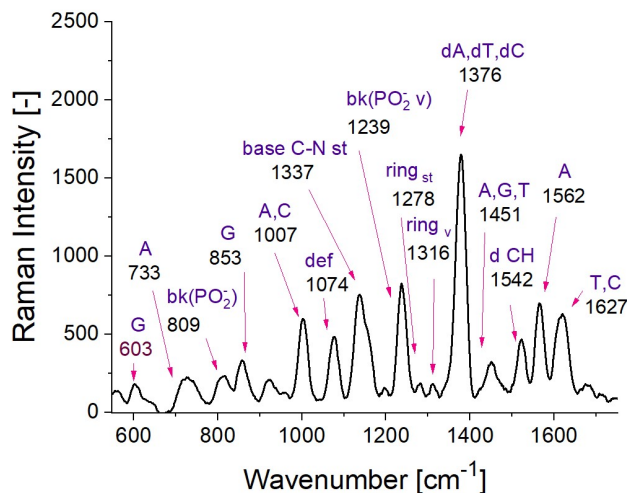
Figure 4. SERS spectrum of DNA on gold-epoxy nanocomposites obtained with 633 nm excitation.

Conclusions

Two application areas were demonstrated for the introduced gold/epoxy surface nanocomposites, namely LSPR sensors and SERS substrates. Our proposed fabrication technology has the following distinct advantages compared to other technologies: 1) Controlled synthesis: the particle size and interparticle distance can be precisely controlled in a fixed hexagonal distribution, and thus the plasmonic absorption peak (and sensitivity) can be fine-tuned for individual applications (which is important to both LSPR and SERS). 2) Large scale fabrication: the lateral size of the substrate is not limited, sensors with several cm^2 surface area can be easily prepared, and the nanoparticle size/distribution is homogenous on the whole surface. 3) Robustness: the prepared nanocomposite – gold nanoparticle arrangement on fixed on epoxy pillars – is completely stable, there is no particle removal exposed to fluidic environments. More detailed information regarding the fabrication and application of these surface nanocomposites can be found in our previous publications [1,4,5].

Acknowledgments

References

[1] Attila Bonyár, "Label-Free Nucleic Acid Biosensing Using Nanomaterial-Based Localized Surface Plasmon Resonance Imaging: A Review", ACS Appl. Nano Mater. 2020, 3, 9, 8506–8521.

[2] I Rigó, M Veres, T Váczi, E Holczer, O Hakkel, A Deák, P Fürjes, "Preparation and Characterization of Perforated SERS Active Array for Particle Trapping and Sensitive Molecular Analysis" Biosensors 9 (3), 93, 2019.

[3] I Rigó, M Veres, Z Pápa, L Himics, R Öcsi, O Hakkel, P Fürjes, "Plasmonic enhancement in gold coated inverse pyramid substrates with entrapped gold nanoparticles", Journal of Quantitative Spectroscopy and Radiative Transfer, 107128, 2020.

[4] Tomáš Lednický, Porous Alumina Assested Fabrication of Nanostructured Layers For Optical Applications, PhD Thesis, Brno, Czech Republic, 2020.

[5] Tomáš Lednický and Attila Bonyár, "Large Scale Fabrication of Ordered Gold Nanoparticle–Epoxy Surface Nanocomposites and Their Application as Label-Free Plasmonic DNA Biosensors". ACS Appl. Mater. Interfaces, 12(4), 4804-4814, 2020.

[6] Guy, R. A.; Xiao, C.; Horgen, P. A. Real-Time PCR Assay for Detection and Genotype Differentiation of Giardia Lamblia in Stool Specimens. J. Clin. Microbiol. 2004, 42 (7), 3317–3320. https://doi.org/10.1128/JCM.42.7.3317-3320.2004.

[7] Spiga, F. M.; Bonyár, A.; Ring, B.; Onofri, M.; Vinelli, A.; Sántha, H.; Guiducci, C.; Zuccheri, G. Hybridization Chain Reaction Performed on a Metal Surface as a Means of Signal Amplification in SPR and Electrochemical Biosensors. Biosens. Bioelectron. 2014, 54, 102–108. https://doi.org/10.1016/j.bios.2013.10.036.

[8] Edyta Pyrak, Aleksandra Jaworsk and Andrzej Kudelski, "SERS Studies of Adsorption on Gold Surfaces of Mononucleotides with Attached Hexanethiol Moiety: Comparison with Selected Single-Stranded Thiolated DNA Fragments", Molecules, 24(21), 3921, 2019.

[9] Gergo Peter Szekeres and Janina Kneipp, "SERS Probing of Proteins in Gold Nanoparticle Agglomerates", Front. Chem., 7, 30, 2019.

Concentration dependent pair-correlation in amorphous $Si_{1-x}Ge_x$ layers revealed by micro-combinatorial TEM

Ildikó Cora, János L. Lábár, György Sáfrán

Institute for Technical Physics and Materials Science, Centre for Energy Research, Konkoly-Thege street 29-33, H-1121 Budapest, Hungary

*Corresponding author: György Sáfrán, e-mail: safran.gyorgy@energia.mta.hu

Keywords: concentration dependent atomic distance, amorphous SiGe, gradient combinatorial sample, whole concentration range, Vegard's rule-like behaviour

Introduction

Our aim was to effectively TEM study the pair-correlation properties ie. average distances of adjacent atoms of a-Si-Ge as a function of Ge concentration in amorphous $Si_{1-x}Ge_x$ layers at the entire composition range. We applied micro-combinatory based on the "one-sample concept" in which a gradient sample was prepared and studied in a single TEM grid representing a whole binary system A_xB_{1-x} (x=0...1) [i, ii]. Thanks to all-in-one feature of the µ-combinatorial TEM specimen no need for laborous preparation, replacement and study of a series individual samples. Beside effectivity a specific advantage of µ-combinatory is that various compositions are formed and investigated side by side, within a single TEM grid that provides superior reproducibility and direct comparison for EDS and SAED measurements.

Experimental

8 nm thick Si-Ge composition spread samples have been deposited by dual DC magnetron sputtering onto Czochralsky-grown NaCl single crystals in a stainless steel UHV vacuum system of $3x10^{-8}$ mbar base pressure. The freshly cleaved substrates were mounted inside the micro-combinatorial device that was introduced into the vacuum chamber through an airlock. After evacuation $3x10^{-3}$ mbar Ar gas was introduced and the gradient SiGe samples were deposited by the two (Si and Ge) power-regulated magnetron sources through a 100 µm wide slot that was sweeping above the substrate The combinatorial layer track was 1mm wide and 2.5 mm long that fits to the view field of the TEM. The length of the track condensed 3 sections: 0.5 mm of Si, 1.5mm of Si-Ge (gradient section) and 0.5 mm of Ge. The preparation technique of µ-combinatorial samples was described, in detail, earlier [ii]. After removal from the vacuum system the samples were wet-stripped from the NaCl and placed on Cu TEM grids with rectangular mesh so that the gradient line was oriented diagonally to the grid bars. This assured that none of the compositions were masked out by the grid bars.

The composition spread SiGe sample was investigated by a conventional PHILIPS CM20 200kV TEM equipped with a BRUKER SDD EDS system and a 300kV JEOL 3010 HRTEM of 0.17 nm point resolution equipped with a GATAN TRIDIEM EELS.

During TEM measurements a series of selected area electron diffraction (SAED) patterns were recorded with carefully controlled and reproduced camera length and lens currents along the gradient film representing various Si-Ge compositions. The local composition was determined with energy Dispersive Electron Spectrometry (EDS) by a Bruker Si-drift detector system. The intensity distribution of SAED-s were determined with help of the software "ProcessDiffraction" [iii] and the nearest atomic distances in the amorphous Si-Ge were calculated and plotted as a function of the elemental composition.
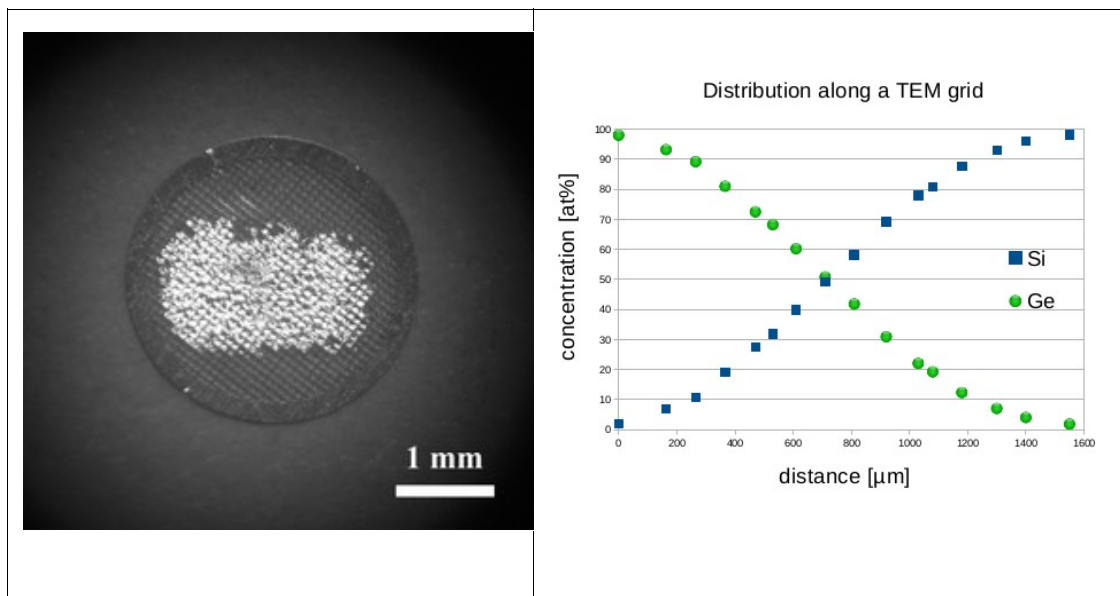
Fig. 1. (a) Overview of an ultrathin (8 nm) concentration-spread µ-combinatorial SiGe sample deposited on Mo TEM grid. The 1x2 mm^2 sized layer consists of a 1000 µm long concentration gradient Si-Ge track enclosed by 250 µm long tracks of pure Si and Ge. (b) Concentration distribution revealed by EDS along a horizontal scan of the µ-combinatorial TEM specimen shown in (a).

Figure 1 (a) shows the overview of the 1x2 mm^2 size combinatorial Si-Ge sample. It consists of three sections: a 1000 µm long stripe with a concentration gradient enclosed by 250 µm long stripes of pure Si and Ge. The Si-Ge concentration distribution as a function of distance along the TEM grid plotted in Fig.1 (b) was measured by EDS in the TEM. The diagram shows an acceptably linear concentration variation with a gradient of 0.1 at% / µm, except at the transition from single to binary component regions.
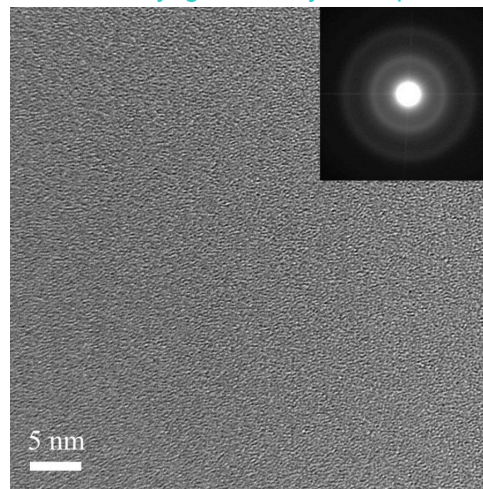
Figure 2. TEM micrograph with SAED inset of the ultrathin 8 nm self-supporting micro-combinatorial amorphous SiGe sample at 50/50 at% composition.

Fig. 2. shows a bright field TEM with a SAED inset at 50/50 at% SiGe composition of the concentration spread sample. Both TEM and SAED represent amorphous structure, that was found at all compositions of the sample.

Atomic distances of a-Si-Ge as a dependence of Ge concentration

Both crystalline Si and Ge form fcc diamond structure with lattice parameters, Si: 0.5392 nm [iv], Ge: 0.5657 nm [v]. Applying Vegard's rule ($a(Si_{1-x}Ge_x) = (1-x)\ a(Si) + x\ a(Ge)$) we calculated the atomic distances (a) of the nearest neighbours in a-Si-Ge as a dependence of Ge concentration. These theoretical atomic distances are represented by the solid line in fig. 3. Deviations from adjacent atomic distances, determined from SAED measurements of the sample of varying composition, from Si are indicated in the same diagram by squares. It is clearly seen, that the squares at the ends of the gradient range (pure Si and pure Ge) show very good fit to the calculated Vegard line, while in the gradient range (mixed compositions) they typically fall above the Vegard line. The measured values, therefore, are "forward" compared to what is calculated - that is, they show an atomic distance corresponding to a higher Ge concentration.

Figure 3. Deviations of adjacent atomic distances from that of Si in an 8 nm thick µ-combinatorial a-SiGe sample, as a function of Ge concentration: determined from SAED measurements (square) and calculated according to the Vegard's rule (solid line).

To explain the difference between the Vegard line and the experimental result, we need to consider the different oxygen affinities and behaviour of the two elements: In the thermal oxidation of amorphous SiGe mixed layers, it was found that ex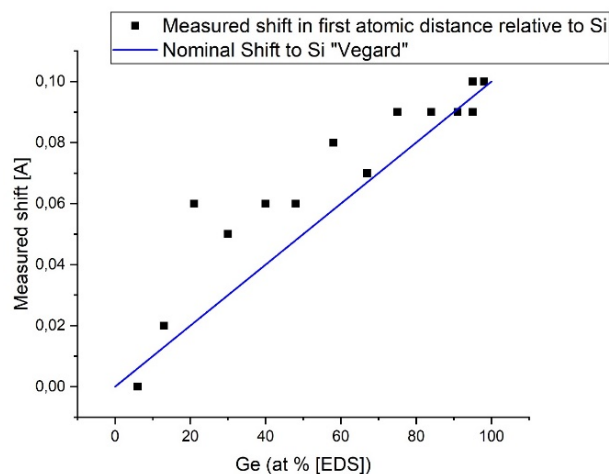clusively SiO_2 is formed on the surface at first, which is accompanied by Si transport and enrichment of Ge under the surface oxide layer. The oxidation of Ge takes place only after the oxidation of the total amount of Si [vi]. It is to note that the selective oxidation mechanism also has technological importance; proposed to form an ultra-thin Ge-rich SiGe layer in CMOS-SOI technology [vii, viii, ix]. In the present study, we concluded that, similarly to the above, selective oxidation of Si took place in the combinatorial SiGe thin film under normal environmental conditions. Due to Si bound in SiO_2, the elementary Si / Ge ratio shifted in the Ge-rich direction, obviously, this caused the deviation of the result measured by SAED from the Vegard rule (Figure 3). It is to note that the layer showed an oxygen content of up to 20% as measured in TEM by EDS. It is easy to see that in an ultra-thin sample of 8 nm in thickness a few atomic layers (~ 1 nm) of native SiO_2, preferably formed on the two free surfaces may bind a significant proportion of Si, hence changing the elemental Si / Ge ratio in the Ge-rich direction.

Conclusion

The average adjacent atomic distances were revealed in the entire composition range as a function of Si-Ge composition. They follow the Vegard's rule in the trend, but due to selective oxidation of Si, the diagram advances towards the values characteristic of Ge-rich compositions.

Acknowledgements

References

[1] G. Sáfrán Hung. Patent, P 15 00500 (2015)

[1] G. Sáfrán, "One-sample concept" micro-combinatory for high throughput TEM of binary films Ultramicroscopy, 187 (2018) 50–55

[1] J.L. Lábár , Ultramicroscopy 103 (2005) 237–249
[1] PCPDFWIN powder diffraction files ver. 2.01, November 1998, #PDF 80-0018
[1] PCPDFWIN powder diffraction files ver. 2.01, November 1998, #PDF 04-0545

[1] Xue, Z. Y., Di, Z. F., Ye, L., Mu, Z. Q., Chen, D., Wei, X., … Wang, X. (2014). Study of Ge loss during Ge condensation process. Thin Solid Films, 557, 120–124.
[1] Tezuka, T.; Sugiyama, N.; Mizuno, T.; Suzuki, M.; Takagi, S.-i. A Novel Fabrication Technique of Ultrathin and Relaxed SiGe Buffer Layers with High Ge Fraction forSub-100nm Strained Silicon-On-Insulator MOSFETs. Jpn. J. Appl. Phys. 2001, 40, 2866–2874.

[1] Lim, Y. S.; Jeong, J. S.; Lee, J. Y.; Kim, H. S.; Shon, H. K.; Kim, H. K.; Moon, D. W. A Study of the Oxidation Behavior and the Postannealing Effect in a Graded SiGe/Si Heterostructure. J. Electron. Mater. 2002, 31, 529–534.

[1] *Riley, L. S.; Hall, S. X-Ray Photoelectron Spectra of Low Temperature Plasma Anodized Si0.84Ge0.16 Alloy on Si(100): Implications for SiGe Oxidation Kinetics and Oxide Electrical Properties. J. Appl. Phys. 1999, 85, 6828–6837.*

Preparation and Characterization of Mixed Metal Oxide Layers using Reactive Combinatorial Sputtering

Z. Labadi,[1*] P. Petrik[1], M. Georghe[2], C. Moldovan[3], M.Fried[1,4]

[1]*Centre for Energy Research, Institute of Technical Physics and Materials Science, 1121 Budapest, Konkoly Thege Miklós út 29-33, Hungary*
[2]*NANOM MEMS SRL, Râsnov, Romania*
[3]*National Institute for Research and Development in Microtechnologies, Bucharest, Voluntari, Romania*
[4]*Institute of Microelectronics and Technology, Óbuda University, Tavaszmezo u. 17, H-1084 Budapest, Hungary*

Abstract

Combinatorial DC sputtering method of metal oxides is presented onto a 30x30cm substrate. Specifically tungsten a molybdenum oxides were deposited and characterized for electrochromic and sensoric purposes. Mapping ellipsometry combined with RBS proves the presence of the continuous composition range in the layers. Samples of amorphous character were tested for electrochromic properties in organic electrolyte. Combinatorial deposition of non-stoichiometric suboxides for VOC gas sensing also presented.

Keywords: sputtering, electrochromism, gas sensors

Introduction

The physical, chemical and structural properties of the cutting-edge materials are strongly dependent on their composition. Using the combinatorial material synthesis approach, materials libraries can be produced in one experiment that contain the full composition range on a single substrate. We use pulsed mode reactive DC sputtering for preparation and Spectroscopic Ellipsometry (SE), RBS-Rutherford Backscattering Spectrometry (RBS) Transmission Electron Microscopy (TEM) forlayer characterization. These methods can help us to search more efficient advanced functional materials for electrochromic and gas sensing properties.

Experimental

Reactive (in Ar-O_2 plasma) W- and Mo-target were placed separately into the sputtering chamber and a proper single axis movement program of the 30x30 cm glass substrates ensured the composition graded final layer from the two (W and Mo) separated targets. (Fig. 1.)
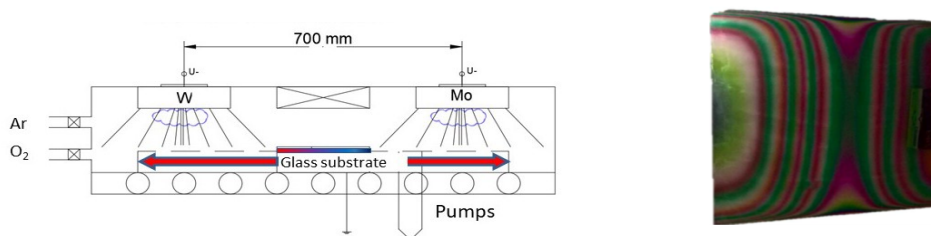
Figure 1. Schematic draw of the combinatorial deposition and layout of a combinatorial layer. Newtonian rings indicate thickness gradient

Results and discussion

Figure 2. shows the ellipsometric mapping of the combinatorial layer (a) together with the schematic optical model (b), while Figure 2c shows the composition of the layer alongside the substrate movement axis. It can be seen from these figures that the layer contains the full compositional range of the MoO_3- WoO_3 binary oxide system.
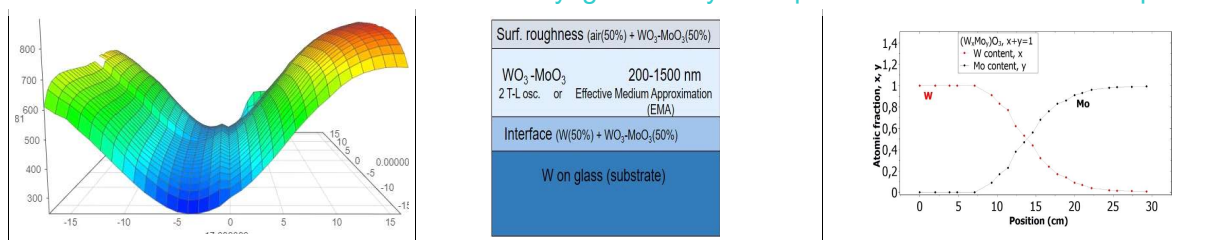
Figure 2. Ellipsometry mapping and optical model of the combinatorial layer (a,b) and lateral composition curves taken by RBS (c)

The layer thicknesses are in the 300-800nm range. Since the number of the uniaxial movenent cycles during the deposition was 1750, no sublayers are expected in the structure.

Figure 3. shows the cross-sectional TEM micrographs of the deposited oxide layers. Presence of the amorphous phase can be seen in the electron diffraction pattern.
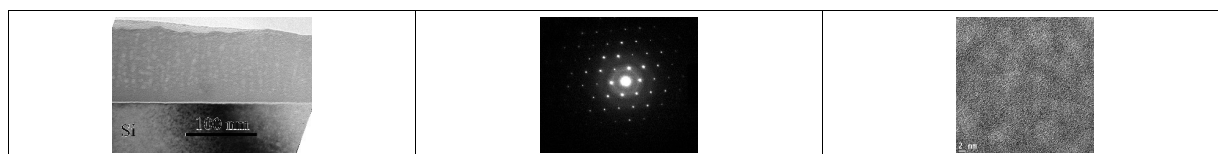
Figure 3. (a) Cross-sectional TEM of the amorphous MoO3 layer (Ar/Ox =40/25 P=100W) Note the porous structure (b)Electron diffraction pattern shows amorphous rings (c) HI-RES TEM of the amorphous MoO3

Figure 4. shows the coloured and bleached state of the (Mo,W) oxide layer in 0,1M LiClO4 – propylene carbonate solution. The deposited sample series makes possible to measure the coloration efficiency

$$CE(\lambda) = \Delta OD(\lambda) / q \quad cm^2 \, C^{-1}$$

where $\Delta OD(\lambda)$ represents the change in single-pass, transmitted optical density at the wavelength of interest λ, because of transfer of charge q of the mixed oxide. This parameter can be measured in the full visible wavelength range, and the combinatorial approach allows 2% composition resolution.
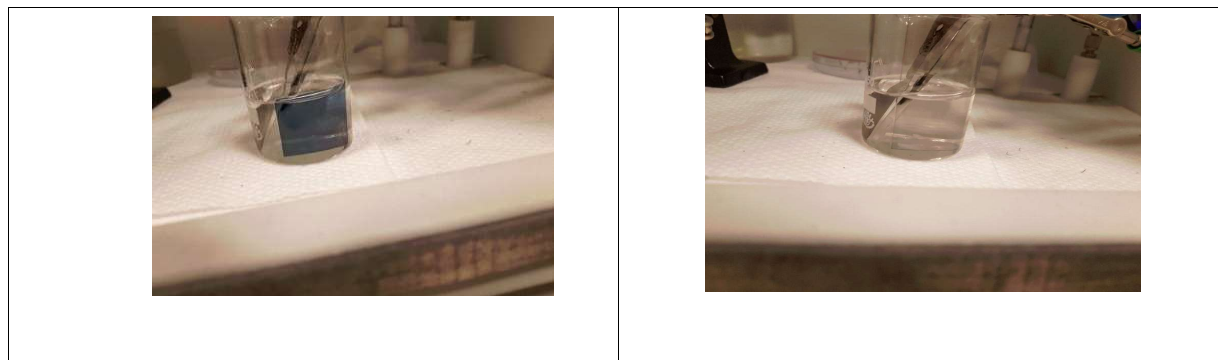
Figure 4: Coloured and bleached state of the (W,Mo) oxide film

Combinatorial samples were also deposited under oxygen depleted conditions. Figure 5 shows the electron dispersive spectrum of the suboxides.
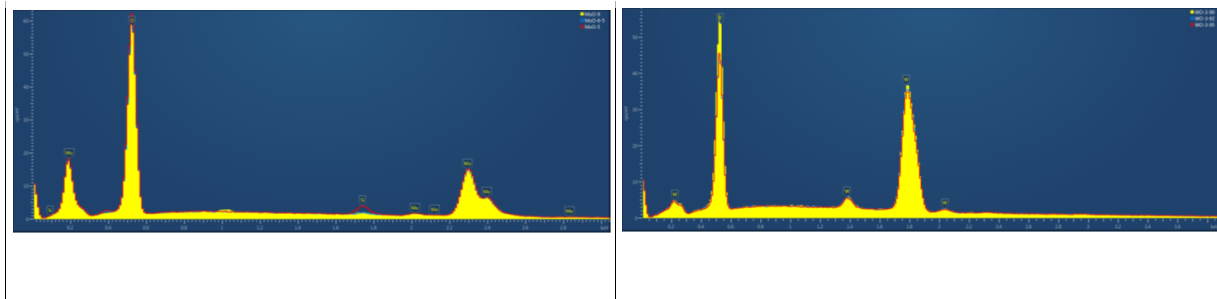
Figure 5. EDS spectra of stoichiometric oxides and suboxides of W and Mo

Semi-quantitative analysis shows 10% oxygen vacancy

The non-stoichiometric samples are tested for VOC gas sensing properties (benzene and formaldehyde sensing).

Acknowledgement

References

[1] M. Fried, R. Bogar, Z. Lábadi, Z. Zolnai: *Combinatorial Investigation of WO3–MoO3 Mixed Layers by SE*; ICSE-8, 8. Int. Conf. on Spectroscopic Ellipsometry, 2019, Barcelona, Spain, oral presentation , submitted to Thin Solid Films

Detecting short-chain thiol binding on CTAB-stabilised gold nanorods at single particle level

Dániel P. Szekrényes[1*], Dániel Zámbó[2], Zsolt Zolnai[1], Norbert Nagy[1] and Andras Deák[1]

[1]*Institute of Technical Physics and Material Science, Centre for Energy Research, Budapest, H-1121 Hungary*

[2]*Institute for Physical Chemistry and Electrochemistry, Leibniz Universität Hannover, Hannover, Germany*

Deeper understanding the binding of thiol molecules on CTAB-capped gold nanorods enables the rational tuning of colloidal interactions. In this study, I would like to present my last results on the adsorption of short thiol-containing molecules on gold nanorods. It is shown that plasmon peak broadening originated from the increasing chemical interface damping (CID) combined with the corresponding peak shift provide information on the ligand exchange process at the single particle level. Based on the findings, the accumulation of negatively charged 3-mercaptopropionic acid (MPA) is reduced compared to that of the positively charged cysteamine because of the interaction of the given thiol-ligand and the native CTAB layer. While cysteamine readily replaces CTAB, the adsorption of MPA leads to a self-limiting process.

Keywords: gold nanoparticles, self-assembly, plasmonics, single particle spectroscopy

Introduction

Ligand exchange using thiol-containing ligands is one of the most widespread procedure for imparting functionality to gold nanoparticles.[1] The majority of gold nanorod syntheses utilise CTAB as a stabilising ligand.[2,3] Thus, the interaction between the thiol-molecule and the native CTAB plays a central role in surface modification. The binding can be easily monitored by spectroscopic measurements, since the optical response of the particles is extremely sensitive on the dielectric properties of the near-field region.[4] In this work, two molecules (namely cysteamine and 3-mercaptopropionic acid) are used for ligand exchange and the modified particles are optically investigated at the ensemble and single particle levels as well[5]. By fitting the scattering spectrum of an individual gold nanorod with a Lorentzian-function the plasmon resonance energy and the damping of the dipole-oscillator model can be determined. The linewidth characterises the entire surface of the particle, while peak shift provides information on the ligand replacement just at the tips of the rod[6].
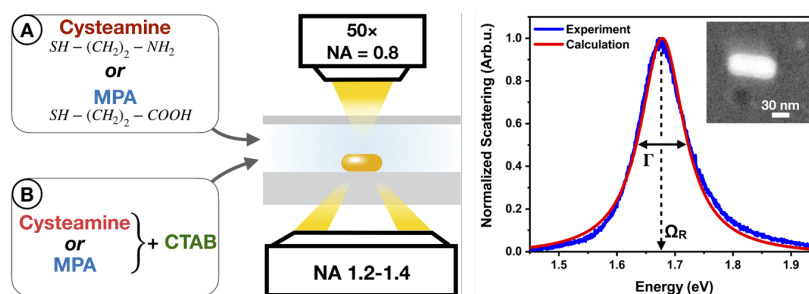

Figure 1: The schematics of the performed experiments without (A) and in the presence of CTAB (B). The obtained scattering spectra were fitted using a Lorenzian-function in order to calculate the resonance energy and the plasmon damping.

Experimental section

Gold nanorods synthetised in this study (24 x 76 nm) were prepared according to a previously published protocol[2]. The surface modification of the CTAB-capped was carried out using similar sized but oppositely charged short-chain thiol ligands (3-mercaptopropionic acid (MPA), cysteamine). The ligand exchange procedure was monitored on the ensemble level by Vis spectrometry and electrophoretic mobility measurments. To gain a deeper insight into the surface modification process *in situ* single particle scattering experiments were performed in a liquid cell using an abberation corrected imaging spectrometer coupled with a dark-field microscope operated in trans-illumination mode.[5]

Results

In our earlier published work[7], the ligand exchange of cysteamine on CTAB-covered gold nanorods was investigated at ensemble and single particle levels as well. It was confirmed that cysteamine forms a well-definded patch at the tips of the gold nanorods which was directly evidenced by AFM measurements and was indicated by the saturation of plasmon peak blueshift and electrophoretic mobility.
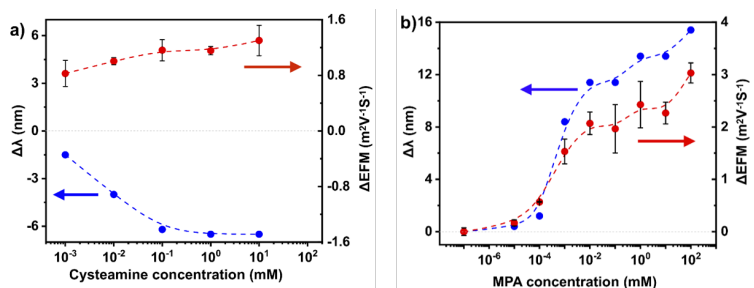
Figure 2: Plasmon peak shift and electrophoretic mobility changes upon adding different concentration of (a) cysteamine and (b) MPA

As shown in Figure 2.a the blueshift and the electrophoretic mobility converge to a limtiting value as a consequense of site-selective binding of cysteamine in agreement with our earlier findings. Interestingly, the attached MPA increases the electrophoretic mobility and causes a redshift (Figure 2.b) which may indicate the accumulation of CTAB at the surface of the nanorods due to electric interactions. In order to get a deeper understanding of the ligand exchange and to corroborate the proposed mechanism of MPA-binding single particle spectroscopy experiments were performed without and in the presence of CTAB as well.
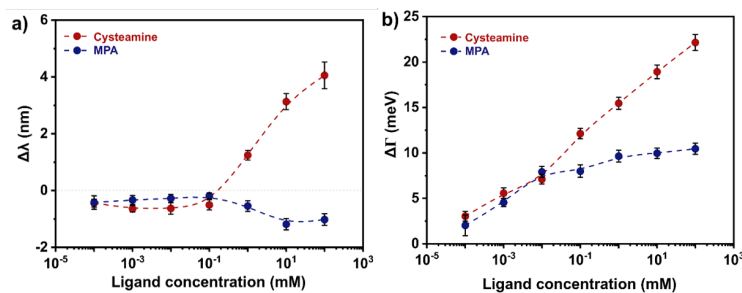
Figure 3: (a) Longitudinal resonance peak shift and (b) broadening obtained for different concentration of cysteamine and MPA

The resonance wavelength and damping change values can be seen in Figure 3. for the case where CTAB was removed. Although the peak position trends were opposite compared to ensemble measurements, the increasing damping indicates the binding of thiol ligands to the gold surface. Figure 3.b also shows the inhibited accumulation of MPA from 10^{-2} mM ligand concentration presumably because of the attractive interaction with the remaining CTAB.
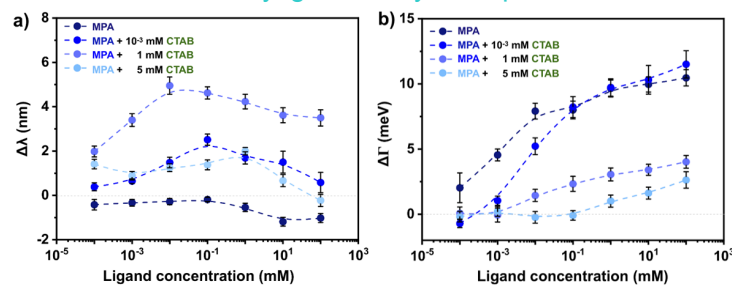
Figure 4: (a) Longitudinal plasmon resonance shift and (b) broadening induced by MPA-addition at different background CTAB concentration

As can be seen in Figure 4, *in situ* MPA-adsorption experiments were carried out with different CTAB concentrations. The magnitude of the redshift is clearly proportional to the bulk CTAB concentration up to the critical micellar concentration of CTAB (cmc = 1 mM). The amount of accumulated MPA was suppressed with increasing CTAB concentration which indicates the self-limiting process of the MPA adsorption (Figure 4.b).

Acknowledgement

References

(1)   Burrows, N. D.; Lin, W.; Hinman, J. G.; Dennison, J. M.; Vartanian, A. M.; Abadeer, N. S.; Grzincic, E. M.; Jacob, L. M.; Li, J.; Murphy, C. J. Surface Chemistry of Gold Nanorods. *Langmuir* **2016**, *32* (39), 9905–9921. https://doi.org/10.1021/acs.langmuir.6b02706.

(2)   Ye, X.; Zheng, C.; Chen, J.; Gao, Y.; Murray, C. B. Using Binary Surfactant Mixtures To Simultaneously Improve the Dimensional Tunability and Monodispersity in the Seeded Growth of Gold Nanorods. *Nano Letters* **2013**, *13* (2), 765–771. https://doi.org/10.1021/nl304478h.

(3)   Jia, H.; Fang, C.; Zhu, X.-M.; Ruan, Q.; Wang, Y.-X. J.; Wang, J. Synthesis of Absorption-Dominant Small Gold Nanorods and Their Plasmonic Properties. *Langmuir* **2015**, *31* (26), 7418–7426. https://doi.org/10.1021/acs.langmuir.5b01444.

(4)   Mayer, K. M.; Hafner, J. H. Localized Surface Plasmon Resonance Sensors. *Chem. Rev.* **2011**, *111* (6), 3828–3857. https://doi.org/10.1021/cr100313v.

(5)   Szekrényes, D. P.; Kovács, D.; Zolnai, Z.; Deák, A. Chemical Interface Damping as an Indicator for Hexadecyltrimethylammonium Bromide Replacement by Short-Chain Thiols on Gold Nanorods. *J. Phys. Chem. C* **2020**, *124* (36), 19736–19742. https://doi.org/10.1021/acs.jpcc.0c04629.

(6)   Foerster, B.; Rutten, J.; Pham, H.; Link, S.; Sönnichsen, C. Particle Plasmons as Dipole Antennas: State Representation of Relative Observables. *The Journal of Physical Chemistry C* **2018**, *122* (33), 19116–19123. https://doi.org/10.1021/acs.jpcc.8b06350.

(7)   Szekrényes, D. P.; Pothorszky, S.; Zámbó, D.; Osváth, Z.; Deák, A. Investigation of Patchiness on Tip-Selectively Surface-Modified Gold Nanorods. *The Journal of Physical Chemistry C* **2018**, *122* (3), 1706–1710. https://doi.org/10.1021/acs.jpcc.7b11211.

How to overcome the uncertainties of polynomial fitting in contact angle determination?

E. Albert[1], B. Tegze[1], Z. Hajnal[2], D. Zámbó[2], D.P. Szekrényes[2], A. Deák[2], Z. Hórvölgyi[1], N. Nagy[2*]

[1]*Budapest University of Technology and Economics, Department of Physical Chemistry and Materials Science, H-1521 Budapest, Hungary*
[2]*Institute of Technical Physics and Materials Science, Centre for Energy Research, P.O. Box 49, H-1525 Budapest, Hungary*

In the present work an easily implementable method is introduced for contact angle determination using sessile drops with a missing apex. Instead of fitting the drop-profile itself, the polynomial fitting is applied to the difference between the drop profile and the circumcircle, independently for both sides of the drop. The derivative value of this difference at the contact point is used to correct the slope obtained analytically from the circumcircle.

Keywords: Wetting; Contact angle; Sessile drop; Captive bubble; Polynomial fitting

The polynomial fitting to the profile of a sessile drop is widely used in those cases when the drop apex is not visible. The major disadvantage of this approach is that the resulted contact angle is highly sensitive to the applied polynomial order and the number of pixels to which the polynomial was fitted. In order to overcome these uncertainties, an easily implementable method was introduced.

Circumcircles are constructed independently for the left and right unperturbed parts of the profile. Polynomial is fitted to the vertical difference between the circumcircle and the profile, see Figure 1.
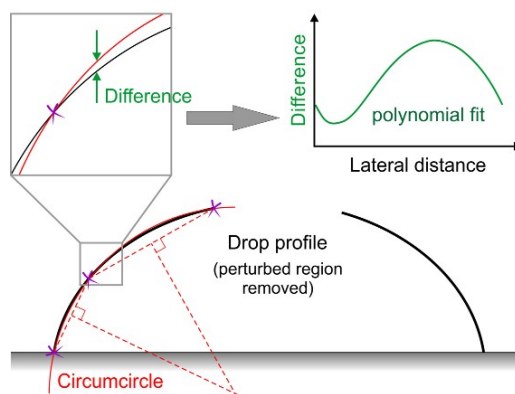
Figure 1. *Schematics of the circumcircle and difference fitting method. Three points are selected from each arc: the endpoints and the point at the half of maximum height. Circumscribed circles that pass through these points are constructed independently and polynomial is fitted to the difference between the circle and the profile as a function of the lateral distance from the contact point.*

The contact angle is calculated from the sum of the slope of the circumscribed circle and the polynomial curve at the three-phase contact point for each side. The derivative of the circumcircle at the contact point can be calculated analytically. The slope of the polynomial curve at the contact point does not change significantly with the contact angle or with the drop volume.

The method was validated in the contact angle range of 20°–150° with two different image resolutions (1280 × 1024 and 750 × 600 pixels) by comparing the results to the values calculated by the Young-Laplace fit (Figure 2). The accuracy of the method was found to be ≤0.6° and it does not show significant dependence on the actual contact angle and on the resolution of the captured image. In comparison, the accuracy of the most sophisticated polynomial method is ≥1°.

Needle-in-drop measurements were carried out on a thermal SiO$_2$ surface for demonstration the capability of the present method (Figure 3). Two syringes were applied with different needle diameter and the determined contact angles were in good agreement considering their standard deviation.

The method improves the accuracy of the evaluation of the needle-in-drop measurements in sessile drop, captive bubble, electrowetting, and electrodewetting experiments.
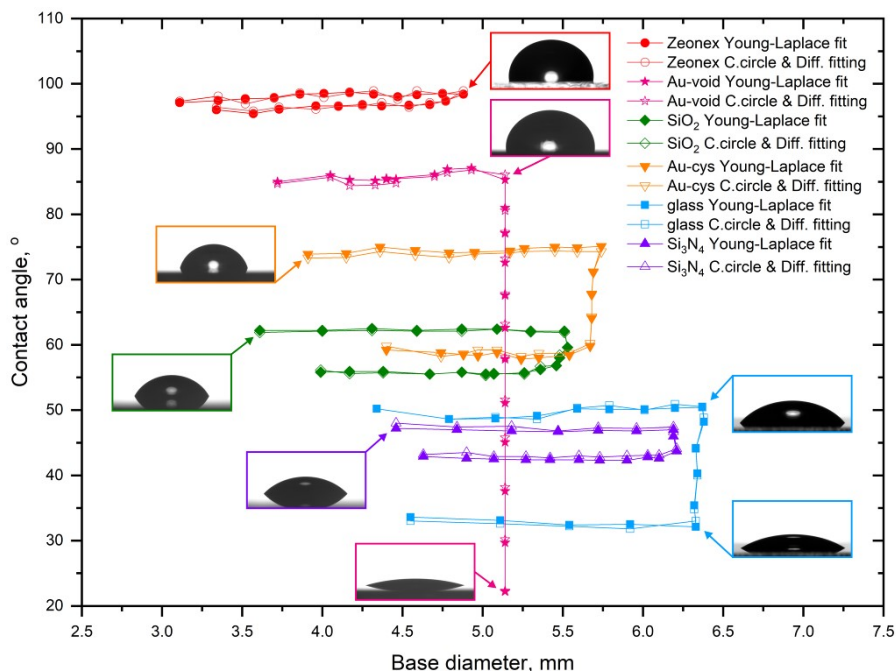
Figure 2. *Contact angles as a function of the drop's base diameter. The values determined by the Young-Laplace fit are shown by filled markers. The hollow markers designate the values determined by the proposed circumcircle and differential fitting.*
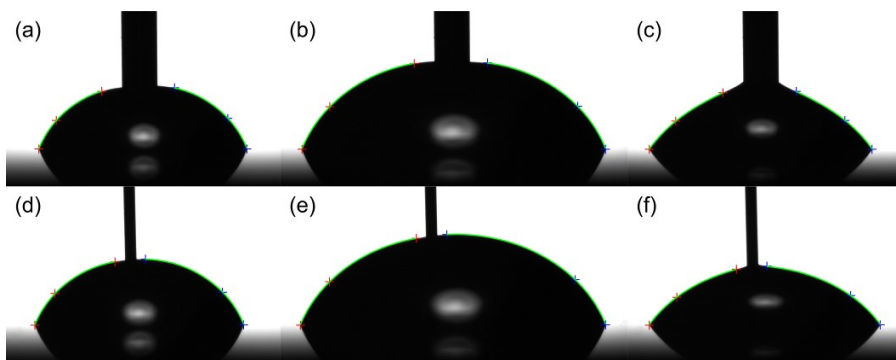
Figure 3. *Evaluated images of water droplets with the volume of 10 µL (a,c,d,f) and 30 µL (b,e) captured in the advancing (a,b,d,e) and the receding phase (c,f). The measurements were carried out using two different needles with the diameter of 0.718 mm (a-c) and 0.235 mm (d-f). The red and blue crosses designate the points for the circumcircle construction, the green curves show the resulted profile after difference fitting.*

References

[1] E. Albert, B. Tegze, Z. Hajnal, D. Zámbó, D. P. Szekrényes, A. Deák, Z. Hórvölgyi, N. Nagy: Robust Contact Angle Determination for Needle-in-Drop Type Measurements, ACS Omega **4**, 2019, 18465-18471

A new effect observed on superhydrophilic surfaces using the capillary bridge probe method

N. Nagy[1*]

[1]*Institute of Technical Physics and Materials Science, Centre for Energy Research, P.O. Box 49, H-1525 Budapest, Hungary*

Utilizing the unique properties of the recently introduced capillary bridge probe method, water contact angles were determined on lightly corroded glass surfaces. A new observation was obtained in these complete wetting situations: the receding contact line starts to advance again during the increase of the bridge length.

Keywords: Wetting; Contact angle; Capillary bridge; Superhydrophilic surface; Glass corrosion

Introduction

Measurement of low contact angles is challenging. The developed indirect Capillary Bridge Probe method combines the accuracy of the Wilhelmy method and the general usability of the sessile drop method without their limitations. The method is based on the use of a liquid bridge as a probe: the capillary bridge of the test liquid is stretched between the rim of the base of a cylinder and the investigated surface under equilibrium conditions. The advancing contact angle on the sample can be measured during the stepwise decrease of the bridge length. The receding contact angle is determined during the retraction of the cylinder. The contact angle is calculated from Delaunay's analytical solution, while the necessary parameters are obtained from the measured capillary force and from the automated analysis of the captured image of the liquid bridge. The bridge is formed from a pendant drop. This unique feature ensures that the advancing contact line finds dry (not prewetted) surface.

The readvancing phase

A new effect was observed during the measurements on freshly acid-cleaned glass surfaces, *i.e.* in complete wetting situations. The receding contact line starts to advance again during the increase of the bridge length, see Figure 1.
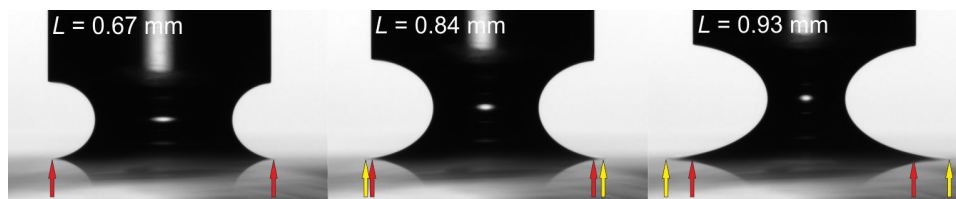
Figure 1. *Images of a water capillary bridge taken during the retraction of the cylinder. The receding contact line starts to advance again after a given bridge length (L). The capillary bridge was formed on a glass slide treated freshly in sulphuric acid. Note that images show equilibrium states, not snapshots of a dynamic process.*

The measured capillary force does not exhibit hysteresis. The contact radius started to increase in the retraction phase, around the bridge length corresponding to bridge formation (Figure 2a). It can be observed in Figure 2b that the advancing and receding contact angles are equal within their standard deviation: $4.7° \pm 0.3°$ and $4.5° \pm 0.3°$, respectively. The measured contact angle in the readvancing phase, *i.e.* the readvancing contact angle is much lower, its value is $1.0° \pm 0.1°$. When the receding contact line starts to advance again, it finds prewetted surface, therefore the resulted contact angle is much smaller.

Figure 2. (a) *Contact radius as a function of the bridge length measured on a glass surface treated in concentrated sulfuric acid.* **(b)** *Contact angle on the glass surface versus the contact radius. Advancing and receding contact angles are equal, while the readvancing contact angle is lower, because the readvancing contact line finds prewetted surface.*

Corroded glass surfaces

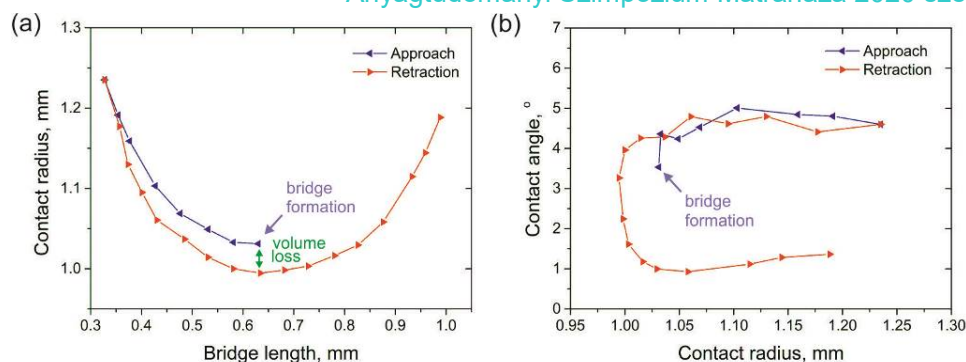Hereafter, lightly corroded glass slides were investigated: how does the water contact angle change as a function of the exposure time to air. Microscope glass slides were cleaned and soaked in 3:1 Piranha-solution. The measurement was started directly after the cleaning process on a glass slide, while other samples were soaked for four days at room temperature. The samples were measured periodically in different positions, and they were left in the humid atmosphere (94%) of the sample chamber between the measurements.

The advancing and receding contact angles were determined to be equal ($3.6° \pm 0.1°$ and $3.6° \pm 0.4°$, respectively) by the first measurement. Their values increase (surface hydroxyl group density decreases) but remain equal for ca. 150 min, and finally significant hysteresis can be observed, while the readvancing phase disappears (increasing amount of surface inhomogeneity) On the contrary, the advancing, receding, and readvancing contact angles remain almost unchanged on the soaked sample. A slight increase of ca. 1° can be observed for both after 260 min.
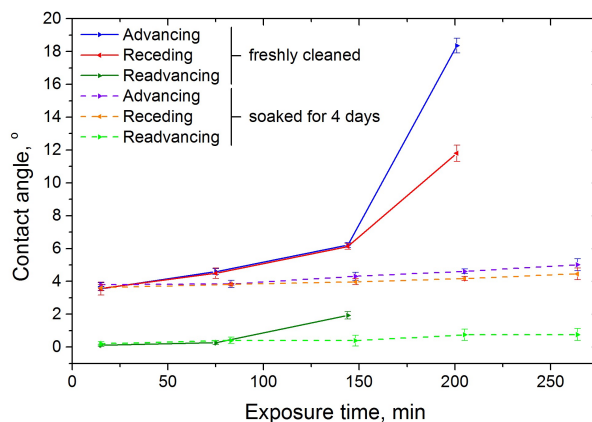
Figure 3. *Advancing, receding, and readvancing contact angles on glass slides as a function of exposure time to humid air (94%). The measurements were performed directly after the cleaning process (continuous lines), and after soaking the sample in ultrapure water for four days (dashed lines). The superhydrophilic character and the readvancing phase of the directly measured surface disappear, while the alteration zone formed by corrosion preserves the super-hydrophilicity.*

References

[1] N. Nagy: Contact Angle Determination on Hydrophilic and Superhydrophilic Surfaces by Using r–θ-Type Capillary Bridges, Langmuir **35**, 2019, 5202-5212

Self-regulating gas dosage for reactive RF sputtering of composition spread Hf oxy-nitride combinatorial layers

György Sáfrán*, Noémi Szász, Gergely Dobrik, Benjámin Kalas and Miklós Serényi

Institute for Technical Physics and Materials Science, Centre for Energy Research, Konkoly-Thege street 29-33, H-1121 Budapest, Hungary

Corresponding author: György Sáfrán, e-mail: safran.gyorgy@energia.mta.hu

Keywords: self-decaying gas inlet, RF sputtering, composition spread layer, ellipsometry

Abstract

We aimed to prepare single sample concept composition-spread metal oxy-nitride layers by reactive radiofrequency sputtering for a highly efficient characterization of their optical properties in a wide range of O/N ratios. Affinity of metals requires oxygen proportion, in the Ar-O-N plasma, be set orders of magnitude lower compared to nitrogen. The required low partial pressure range of oxygen was covered by a new concept self-regulating gas inlet assembly based on a peristaltic pump delivering gas from a finite volume vial. We proved the suitability of our combinatorial method by both energy dispersive spectrometry mapping and ellipsometry of the correlated refractive indices along a 3-component composition-spread HfON sample.

Introduction

Thin layers of metal-oxy-nitrides (MeON) are widely used (Me denotes e.g. Al, Ti, Hf, Si) for wavelength selective coatings of optical elements, smart windows and laser diodes [x]. Their advantageous feature is the tunable refractive index by the proportion of the oxide and nitride components. Our aim was the synthesis of a single, concentration spread combinatorial sample in order to reveal the optical properties of various radiofrequency (RF)-sputtered metal-oxy-nitride layers in a wide range of O/N ratios. Recently „one sample concept" micro-combinatory has been developed [xi] for comprehensive characterization of two components "metal" (Me) films including Mn-Al [xii], Mg-Al [xiii] and Si-Ge [xiv, xv]. The deposition of gradient "Me-Me" samples is performed, through a moving slot, by means of DC magnetron sputtering from two targets of severally controlled power. We made further developments, currently to adapt micro-combinatory to reactive RF sputtering: a composition-spread layer is deposited from a single Me target by RF sputtering, meanwhile the ratio of the reactive components (O and N) in the plasma gas is variedAs we want to cover a composition range of the deposited film from Me-oxide to nitride the oxygen partial pressure has to be varied well below $1\cdot10^{-4}$ mbar. Unfortunately, the common gas dispensers cannot provide both the required low flow rates and fine control of partial pressures. We propose a self-regulating assembly for gas inlet: Oxygen is introduced to the chamber by a peristaltic pump emptying a finite volume reservoir. As oxygen is pumped out, the pressure in the reservoir gradually decreases. If gas is supplied at a constant volume rate from a reservoir of decreasing pressure, the mass transport rate will, as well, decrease. Therefore, the partial pressure of the oxygen gradually decreases towards base pressure of the sputtering chamber, while that of argon and nitrogen is kept constant by using conventional flow meters. A continuous depletion of the Ar-O-N reactive gas mixture in oxygen, during deposition, enables the deposition of composition spread oxy-nitride combinatorial samples.

Materials and methods

According to our experiments an oxygen partial pressure change between $1\cdot10^{-4}$ and $1\cdot10^{-5}$ mbar is suitable to cover a composition range of the deposited layer between Hf-oxide and Hf-nitride. Therefore, a device is required to regulate oxygen injection in this pressure range. The setup of the proposed self-regulating gas inlet assembly is represented by the scheme in figure 1. (a) that shows the sputtering chamber with the attached peristaltic pump connected to the oxygen reservoir (vial).

Prior to reactive RF sputter deposition of combinatorial samples a dedicated experiment was carried out. For this test, our RF sputtering chamber (Leybold Z400) was used. The vial of 48 cm³ volume was filled

with 1 bar oxygen and the volume rate of the peristaltic pump was set to 1 cm^3/min. As the sputtering chamber was evacuated, by a turbo molecular pump, to its base pressure of about $6\cdot10^{-7}$ mbar the peristaltic pump was started and it began to deliver O$_2$ from the vial into the chamber. As oxygen appeared in the chamber, the pressure suddenly increased to $9\cdot10^{-5}$ mbar followed by a continuous decay due to a decrease of the delivered gas from the gradually emptied vial. The pressure in the chamber was measured, as a function of time, until it decreased to $1\cdot10^{-5}$ mbar and then the peristaltic pump was stopped. The elapsed time was 110 minutes. The variation of the pressure in the chamber as a function of pumping time is plotted with full circles, in the diagram of Figure 1 (b). An O$_2$ partial pressure range between $9\cdot10^{-5}$ and $1\cdot10^{-5}$ mbar covered by our gas inlet assembly is considered to be suitable to deposit the designed composition spread Me oxy-nitride samples.

Modelling the gas inlet assembly

In addition to the dedicated experiment peristaltic pumping from a finite volume vial can be modeled by repetitive application of the general gas equation. Let p_{N2} be the pressure of the vial in the nth minute:

$$p_{N2}=p_0(1-v/V)^n \qquad (1)$$

where p_0 is the manifold pressure of the V-volume vial and v volume of the O$_2$ gas pumped out during one minute. The p_{O2} partial pressure change at 1sccm O$_2$ inlet into the vacuum system was determined by the dedicated measurement. It was found to be $0.9\cdot10^{-4}$ mbar right after the start of the peristaltic pump, and with a sudden transient it dropped to $0.8\cdot10^{-4}$ mbar which is considered the initial value. The final pressure of the system was chosen to be 10^{-6} mbar, hence p_{O2} can be estimated as follows:

$$p_{O2}=0.1+8(1-1/V)^n \qquad (2)$$

(n is the elapsed time in minutes)

The pressure change as a function of time, modeled according to equation (2), is plotted with a solid line in Figure 1 (b). It starts at an initial value of $8\cdot10^{-5}$ mbar and shows an asymptotic decrease towards $1\cdot10^{-6}$ mbar. The elapsed time until it reached $1\cdot10^{-5}$ mbar was about 105 minutes. The HfON composition spread layer was deposited onto a 25x10 mm^2 Ge wafer placed behind a shutter with a narrow (1 mm) slot that was swept along the substrate by a stepping motor. The scheme of substrate and shutter is shown in fig.1 a. at the lower part of the chamber. The stepping motor moved the slot by 25 μm per step. The control was performed by a microcontroller, which allowed the speed of shutter to be varied over a wide range. Sputtering was performed under 10 to 1 mixture of high purity nitrogen and argon at a plasma pressure of $2.5\cdot10^{-2}$ mbar. Subsequent to pre-sputtering the target for 10 minutes O$_2$ gas was introduced from the 48 cm^3 vial with 1 bar initial pressure, by the operation of the peristaltic pump. Peristaltic pumping was maintained for 110 min at a volume rate of 1cm^3/min (causing a steady decrease of O$_2$ partial pressure in the chamber from $9\cdot10^{-5}$ to $1\cdot10^{-5}$ mbar), meanwhile, Ar and N pressures were kept constant. The sweeping time of the slot above the substrate was set to be in sync with the duration of O$_2$ inlet.
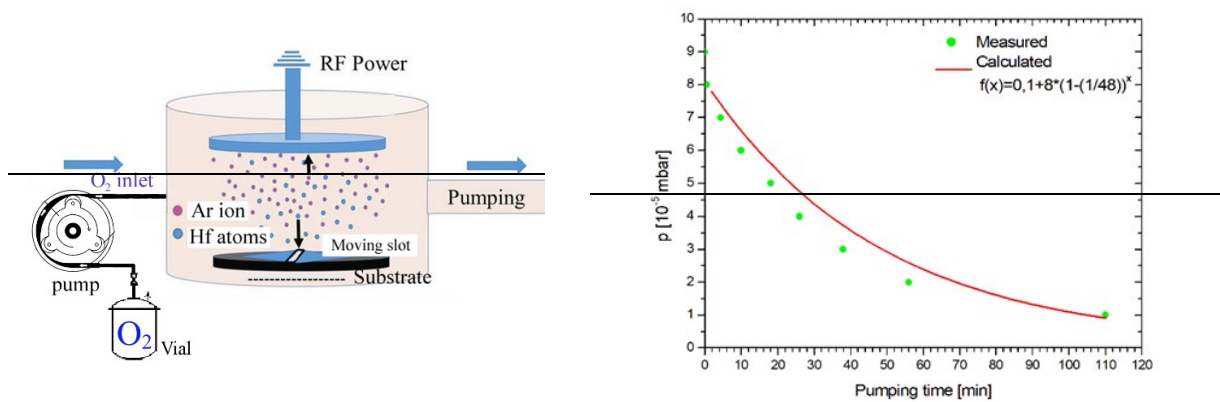

Figure 1. (a) Setup of the self-regulating gas inlet. (b) Variation of oxygen partial pressure in the sputtering chamber during an oxygen inlet experiment: the peristaltic pump was operated at a rate

of 1cm³/min emptying the 48 cm³ vial of 1 bar initial pressure. Measured pressure decay during the experiment (●). Calculated pressure decay according to equation 2 (−).

Sputtering the Hf target in an Ar-O-N reactive gas mixture from which oxygen was gradually depleted resulted in a continuous drop of the O/N ratio in the deposited HfON. The deposit was laterally distributed along the substrate by the sweeping slot, so that a composition spread film was formed covering the range of transition from Hf-oxide to Hf-nitride.

The properties of the combinatorial Hf-oxy-nitride sample prepared as above were investigated by EDS and ellipsometry measurements. For to reveal the effects of the variation of oxygen inlet on the oxygen and nitrogen proportion of the layer the composition was determined along the sample by EDS in a FEI Scios scanning electron microscope using 3 keV probe with 13 nA current The O/O+N ratio as a function of distance along the combinatorial layer is plotted in fig.2.

The optical properties of the combinatorial sample along the substrate were investigated by means of a spectroscopic ellipsometer with a rotating compensator configuration (Woollam-2000DI). The variation of refractive index revealed as a function of distance along the sample is plotted in fig.2. According to the dedicated test the assembly for variable oxygen gas inlet has worked properly.
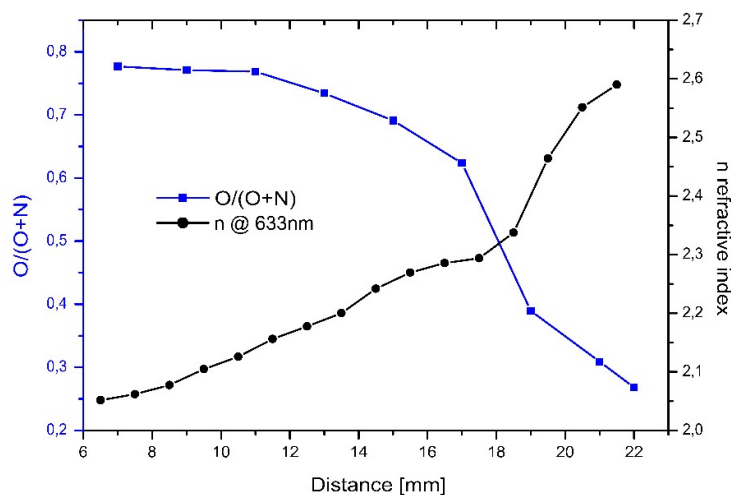

*Figure 2. Variation of O/O+N and refractive index along the combinatorial Hf-O-N sample revealed by EDS (■), and **n** by ellipsometry at 632.8 nm wavelength (●), respectively.*

The covered oxygen partial pressure range between $9 \cdot 10^{-5}$ and $1 \cdot 10^{-5}$ mbar revealed by both measurement and modelling was suitable to deposit a composition spread Me oxy-nitride sample. The correlations of composition of sputtering gas and that of deposited film, as well refractive index variation are revealed and presented in Fig.2. as a function of position along the combinatorial sample. The O/(O+N) ratio curve characteristic to the film composition, measured by EDS, depicted with full squares, shows monotonous decrease along the sample. It is in response to the gradual oxygen depletion of plasma gas during reactive sputtering. O/(O+N) values extending between 0.78 and 0.27 indicates that the combinatorial layer covers a wide composition range of HfON. The correlated refractive index values measured by ellipsometry and evaluated by the methods and parameters of [xvi, xvii] are depicted with full circles. It shows a monotonous transition of n-values between 2.05 and 2.6. Obviously, refractive index variation of the combinatorial sample covers about the entire composition range between stoichiometric HfO_2 [xviii, xix] and HfN [xx, xxi].

The results shown in fig.2 are illustrating that one sample concept combinatorial technique was successfully adapted to reactive RF sputter deposition and that the synthesized combinatorial sample is suitable to a comprehensive characterization of Me-oxy-nitrides in a wide composition range.

References

[i] G. Sáfrán Hung. Patent, P 15 00500 (2015)

[ii] G. Sáfrán, "One-sample concept" micro-combinatory for high throughput TEM of binary films Ultramicroscopy, 187 (2018) 50–55

[iii] J.L. Lábár , Ultramicroscopy 103 (2005) 237–249

[iv] PCPDFWIN powder diffraction files ver. 2.01, November 1998, #PDF 80-0018

[v] PCPDFWIN powder diffraction files ver. 2.01, November 1998, #PDF 04-0545

[vi] Xue, Z. Y., Di, Z. F., Ye, L., Mu, Z. Q., Chen, D., Wei, X., … Wang, X. (2014). Study of Ge loss during Ge condensation process. Thin Solid Films, 557, 120–124.

[vii] Tezuka, T.; Sugiyama, N.; Mizuno, T.; Suzuki, M.; Takagi, S.-i. A Novel Fabrication Technique of Ultrathin and Relaxed SiGe Buffer Layers with High Ge Fraction forSub-100nm Strained Silicon-On-Insulator MOSFETs. Jpn. J. Appl. Phys. 2001, 40, 2866–2874.

[viii] Lim, Y. S.; Jeong, J. S.; Lee, J. Y.; Kim, H. S.; Shon, H. K.; Kim, H. K.; Moon, D. W. A Study of the Oxidation Behavior and the Postannealing Effect in a Graded SiGe/Si Heterostructure. J. Electron. Mater. 2002, 31, 529–534.

[ix] Riley, L. S.; Hall, S. X-Ray Photoelectron Spectra of Low Temperature Plasma Anodized Si0.84Ge0.16 Alloy on Si(100): Implications for SiGe Oxidation Kinetics and Oxide Electrical Properties. J. Appl. Phys. 1999, 85, 6828–6837.

[x] M. Serényi, M. Rácz, T. Lohner, Refractive index of sputtered silicon oxynitride layers for antireflection coating, Vacuum 61(2-4) (2001) 245–249.

[xi] G. Sáfrán, "One sample concept" micro-combinatory for high throughput TEM of binary films, Ultramicroscopy 187 (2018) 50–55. https://doi:10.1016/j.ultramic.2018.01.001

[xii] G. Sáfrán, J. Szívós, M. Németh, A. Horváth, Phase mapping of thin Mn-Al layers by combinatorial TEM. In: Ágnes, Kittel; Béla, Pécz (szerk.) 12th Multinational Congress on Microscopy: MCM 2015, Budapest, Hungary: Akadémiai Kiadó (2015) 559-560.

[xiii] N. Q. Chinh, G. Sáfrán, High strength of ultrafine-grained Al–Mg films and the relevance of the modified Hall–Petch-type relationship MRS COMMUNICATIONS 9 (3) (2019) 1111-1114.

[xiv] T. Lohner, B. Kalas, P. Petrik, Zs. Zolnai, M. Serényi, G. Sáfrán, Refractive index variation of magnetron-sputtered a-Si1-xGex by "one-sample concept" combinatory, Appl. Sci. 2018, 8, 826

[xv] B. Kalas, Zs. Zolnai, G. Sáfrán, M. Serényi, E. Agocs, T. Lohner, A. Németh, M. Fried, P. Petrik, Micro-combinatorial sampling of the optical properties of hydrogenated a- $Si_{1-x}Ge_x$ for the entire range of compositions towards a database for optoelectronics, Scientific Reports, accepted

[xvi] D.A.G. Bruggeman, "Berechnung verschiedener physikalischer Konstanten von heterogenen Substanzen. I. Dielektrizitätskonstanten und Leitfähigkeiten der Mischkörper aus isotropen Substanzen," Ann. Phys. 416(8) (1935) 665–674.

[xvii] T.N. Nunley, N.S. Fernando, N. Samarasingha, J.M. Moya, C.M. Nelson, A.A. Medina, S. Zollner, Optical constants of germanium and thermally grown germanium dioxide from 0.5 to 6.6 eV via a multisample ellipsometry investigation, J. Vac. Sci. Technol. B 34, (2016) 061205

[xviii] https://refractiveindex.info/?shelf=main&book=HfO2&page=Wood

[xix] J. Sancho-Parramon, M. Modreanu, S. Bosch, M. Stchakovsky, Optical characterization of HfO2 by spectroscopic ellipsometry: Dispersion models and direct data inversion. Thin Solid Films, 516(22), (2008) 7990–7995. https://doi:10.1016/j.tsf.2008.04.007

[xx] https://ntrs.nasa.gov/archive/nasa/casi.ntrs.nasa.gov/19820013457.pdf

[xxi] H. Gueddaoui, S. Maabed, G. Schmerber, M. Guemmaz, J. C. Parlebas, Structural and optical properties of vanadium and hafnium nitride nanoscale films: effect of stoichiometry, The European Physical Journal B, 60(3), (2007) 305–312. https://doi:10.1140/epjb/e2006-00350-9